Title:

The integrity of dopaminergic and noradrenergic brain regions is associated with different aspects of late-life memory performance

Authors:

Martin J. Dahl [1,2,*], Shelby L. Bachman [2], Shubir Dutt [2,3], Sandra Düzel [1], Nils C. Bodammer [1], Ulman Lindenberger [1,4], Simone Kühn [4,5,6], Markus Werkle-Bergner [1], & Mara Mather [2]

Affiliations:

[1] Center for Lifespan Psychology, Max Planck Institute for Human Development, 14195 Berlin, Germany

[2] Leonard Davis School of Gerontology, University of Southern California, 90089 Los Angeles, CA, USA

[3] Department of Psychology, University of Southern California, 90089, Los Angeles, CA, USA

[4] Max Planck UCL Centre for Computational Psychiatry and Ageing Research, London, England, and Berlin, Germany

[5] Lise Meitner Group for Environmental Neuroscience, Max Planck Institute for Human Development, 14195 Berlin, Germany

[6] Department of Psychiatry and Psychotherapy, University Clinic Hamburg-Eppendorf, Hamburg, Germany

*** Corresponding author:**

MJD (dahl@mpib-berlin.mpg.de)

Abstract:

Researchers have identified changes in dopaminergic neuromodulation as playing a key role in adult memory decline. Facilitated by technical advancements, recent research has also implicated noradrenergic neuromodulation in shaping late-life memory performance. However, it is not yet clear whether these two neuromodulators have distinct roles in age-related cognitive changes.

Combining longitudinal high-resolution magnetic resonance imaging of the dopaminergic substantia nigra–ventral tegmental area (SN–VTA) and the noradrenergic locus coeruleus (LC) in younger (n = 69) and older adults' (n = 251), we found that dopaminergic and noradrenergic integrity are differentially associated with individual differences in memory performance. While LC integrity was related to better episodic memory across several memory tasks, SN–VTA integrity was linked to working memory. Moreover, consistent with their dense interconnection and a largely shared biosynthesis, dopaminergic and noradrenergic brain regions' integrity were positively related, and correlated with medial temporal lobe volumes. Longitudinally, we found that older age was associated with more-negative change in SN–VTA and LC integrity (time point 1–time point 2; mean delay ~1.9 years). Importantly, changes in LC integrity reliably predicted future episodic memory performance (at time point 3).

These findings support the feasibility of in-vivo indices for catecholaminergic integrity with potential clinical utility, given the degeneration of both neuromodulatory systems in several age-associated diseases. Moreover, they highlight differential roles of dopaminergic and noradrenergic neuromodulatory nuclei in late-life cognitive decline.

Introduction:

Our memory fades as we age [1]. On average, old age is characterized by impaired abilities to retain and manipulate information over shorter time scales—termed working memory [2–4]—and to recollect past experiences within their temporal and spatial context—called episodic memory [1,5,6]. On a neural level, senescent declines in memory have been linked to dopaminergic neuromodulation [7–9] and, more recently, also to noradrenergic neuromodulation [10–12]. The degeneration of catecholaminergic (i.e. dopaminergic and noradrenergic) systems also is a core feature of age-related pathologies, such as Alzheimer's and Parkinson's disease [11,13–18] that are characterized by amnestic impairments [19,20]. However, investigations disentangling the contribution of the two neuromodulators to human memory in aging and disease are scarce.

Neuromodulators are a group of neurochemicals synthesized in circumscribed subcortical nuclei from which they are released throughout the brain via widely branching axonal projections [21]. Dopaminergic neurons are based mainly in the midbrain substantia nigra–ventral tegmental area (SN–VTA) [22], whereas noradrenergic neurons are primarily found in the brainstem locus coeruleus (LC) [23].

There are several mechanistic accounts linking dopaminergic and noradrenergic neuromodulation to aging memory. Computational models posit that catecholamines modulate the input–output relation of neurons (i.e., gain change) which increases the signal-to-noise ratio in neural processing [24] and influences cognition [25–27]. Age-related neurodegeneration of dopaminergic and noradrenergic nuclei thus results in noisier neural information processing (i.e., gain reduction) [8]. Specifically, declining catecholaminergic drive with increasing age is hypothesized to lead to less distinctive cortical representations and senescent memory decline [8,28].

A second mechanism linking dopaminergic and noradrenergic neuromodulation to aging memory is their modulation of prefrontal processing [29]. Lateral prefrontal circuits can represent external stimuli in the absence of sensory stimulation, even in the face of distractors, by means of persistently firing delay cells [30]. Catecholaminergic inputs orchestrate recurrent activity in delay cell circuits that is essential for higher-order cognitive functions, such as working memory [31]. Specifically, the stimulation of dopaminergic D1-receptors and noradrenergic α_{2a}-receptors boosts prefrontal delay activity with an inverted-u dose–response curve [12]. Age-related memory deficits, in turn, have been associated with reduced delay cell firing, which could be partially restored by catecholaminergic drugs [32–35].

Finally, dopamine and noradrenaline modulate hippocampal long-term potentiation (LTP) and long-term depression (LTD) [36–40], which are critical for synaptic plasticity and memory. Initial accounts proposed a ventral tegmental area–hippocampal circuit by which neuromodulatory inputs facilitate the consolidation of salient experiences [36,39,41]. Interestingly, more recent investigations indicate that while the SN–VTA and LC both project to the dorsal hippocampus, the latter sends denser inputs [42–44]. LC neurons also produce dopamine as biosynthetic precursor of noradrenaline [45], and can co-release both catecholamines to modulate hippocampal synaptic plasticity and memory [42,43,46–48]. Older age is characterized by impaired hippocampal plasticity [49,50], likely exacerbated by deficient catecholaminergic innervation from the LC and SN–VTA [51].

Taken together, dopaminergic and noradrenergic neuromodulation mechanistically sculpts senescent memory via several pathways, including gain modulation [8,10], frontal delay activity[30,32], and hippocampal synaptic plasticity [36,47]. Notably, these mechanisms are specified for dopaminergic *and* noradrenergic neuromodulation (gain modulation [24]; delay activity [12]; synaptic plasticity [47]). However, research sampling a broad array of cognitive tasks to identify *unique* associations with late-life memory is lacking. That is, while animal research has demonstrated considerable overlap of

catecholamines at the neural level, the question remains how much dopaminergic and noradrenergic nuclei overlap in their association with behavior.

Comparative studies of catecholaminergic systems in humans were long hampered by technical challenges in reliable non-invasive assessments of the small subcortical nuclei [52,53]. However, recent advances in high-resolution magnetic resonance imaging (MRI) reveal the SN–VTA [17,54] and LC [55,56] as focal hyperintensity on MRI scans. Multimodal post-mortem validation studies suggest this hyperintensity as a marker for catecholaminergic neurons [57–59]. Neuromelanin, a catecholamine-derived paramagnetic pigment accumulating in the LC and SN–VTA [60,61], presumably contributes to the MRI contrast of the nuclei [56,58,59,62,63]. However, also other factors likely play a role, such as the large cellular bodies of catecholaminergic neurons [64,65] that results in a high abundance of ions and water protons [65] as well as a lower macromolecular fraction [66,67]. Importantly, first in-vivo studies suggest an association between the MRI intensity of catecholaminergic nuclei and their functionality [58]. Furthermore, investigations in clinical populations confirm the validity of the imaging approach [17,68–72].

Catecholaminergic nuclei are among the first brain structures to accumulate pathologies in age-associative diseases like Parkinson's and Alzheimer's [13,73,74] and show severe degeneration over the course of these diseases [11,14,16]. In line with this, LC [68–70] and SN–VTA [17,71,72] imaging using dedicated MRI sequences (i.e., Magnetization Transfer [MT], Fast Spin Echo [FSE]) reveals reduced hyperintensities in patients relative to controls. In healthy lifespan samples, initial cross-sectional evidence reveals a negative quadratic relationship between age and catecholaminergic hyperintensity [75–77], whereby lower contrast with advancing age might be linked to impending pathology [68,78,79]. Taken together, recent advances in imaging techniques open the door for comparative non-invasive assessments of catecholaminergic nuclei integrity, which are sensitive for age and disease-related changes [17,54,56,71,72].

In the present study, we took advantage of these new imaging approaches to attempt to disentangle the relative contribution of declining dopaminergic and noradrenergic neuromodulation to aging cognition. We repeatedly assessed cognitive performance and high-resolution MRI in large samples of younger and older adults across multiple time points [80–83]. Furthermore, we leveraged latent-variable modeling of multimodal imaging [84,85] and comprehensive cognitive assessments [85,86] to decrease measurement error and increase generalizability [87]. In sum, the goal of this study was to extend our knowledge about the respective roles of dopaminergic and noradrenergic neuromodulation in late-life memory decline.

Results:

Locus coeruleus and substantia nigra–ventral tegmental area intensity shows high agreement across imaging modalities

We applied a validated semi-automatic procedure [88–92] to extract intensity information of catecholaminergic nuclei from different imaging sequences (FSE, MT+, and MT–; see Methods and Figure S2)—by standardizing MRI intensity in the LC and SN–VTA based on the intensity in an adjacent white matter reference region [55,56,58] (see Figures 1 and 2). Based on earlier post-mortem validations [57–59,69], we interpret individual differences in standardized MRI intensity as proxy for the integrity of catecholaminergic nuclei. Next, we leveraged an established factor structure [88] to integrate intensity information across hemispheres for each imaging sequence and age group (see Figure S3).

Previous in-vivo studies of catecholaminergic nuclei relied on different imaging approaches (mostly MT+ and FSE; [17,54–56]), but there are few comparisons between these MRI sequences, limiting cross-study comparability. Contrasting LC and SN–VTA estimates, we found strong differences across MRI sequences in their average intensity, $\Delta\chi^2(df = 2) = 693.55$; $p < 0.001$ for older adults' LC; $\Delta\chi^2(df = 1) = 657.37$; $p < 0.001$ for older adults' SN–VTA. That is, standardized to a reference region, catecholaminergic nuclei appeared brightest in the MT+, followed by the FSE, and finally the MT– sequences, for older adults' LC (mean [standard error]): MT+, 25.816 (0.304); FSE, 20.144 (0.37); MT–, 6.425 (0.194); for older adults' SN–VTA: MT+, 19.523 (0.235); MT–, 2.979 (0.135). Crucially, despite these mean differences, intensities were highly correlated across imaging modalities, r =0.43–0.621; $p < 0.001$ for older adults' LC; r =0.503; $p < 0.001$ for older adults' SN–VTA (see Figure 3 and S6–8), indicating that these sequences provide convergent information about the same underlying construct (i.e., catecholaminergic nuclei).

We thus aggregated the information shared across imaging modalities by estimating multimodal latent factors expressing LC integrity and SN–VTA integrity (see Figure S4; for comparable approaches and a discussion, see [85] and [84,93]). Such latent variables capture the commonalities across scan modalities while removing the modality-specific measurement error and hence increase statistical power to detect true effects [87]. Model visualizations, model fit, and younger adults' findings are reported in the supplementary information (see Figures S3–4, S6–7, and [94]).

Taken together, we extracted the intensity of the LC and SN–VTA from different MRI sequences sensitive for catecholaminergic nuclei. We found a high agreement in intensities across imaging modalities and thus aggregated across sequences to obtain individual integrity estimates for the two catecholaminergic nuclei.

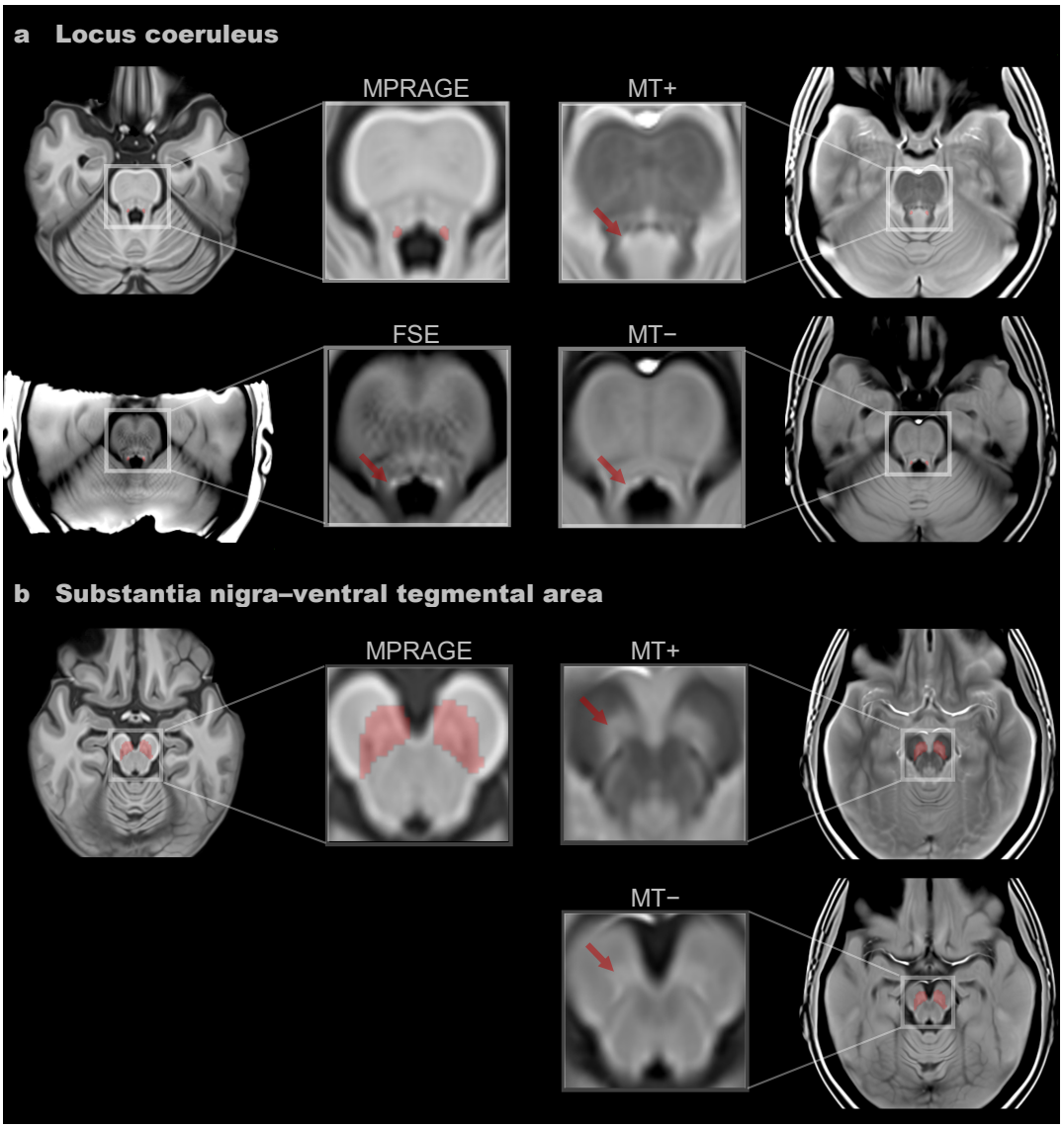

Figure 1. LC and SN–VTA-sensitive magnetic resonance imaging sequences. Hyperintensities corresponding to the (**a**) LC and (**b**) SN–VTA are indicated by red arrows on axial slices of group templates based on a Fast Spin Echo (FSE) sequence, and a Magnetization Transfer sequence, acquired once with a dedicated magnetic saturation pulse (MT+) and once without, resulting in a proton density image (MT–). A Magnetization Prepared Gradient-Echo (MPRAGE) sequence template shows the location of a previously-established LC [68] and SN–VTA [58] volume of interest (red overlays). Note that our FSE sequence only covered the brainstem. All templates were registered to MNI152 0.5mm linear space and are available at [94]. Templates were estimated across age groups. LC, locus coeruleus; SN–VTA, substantia nigra–ventral tegmental area.

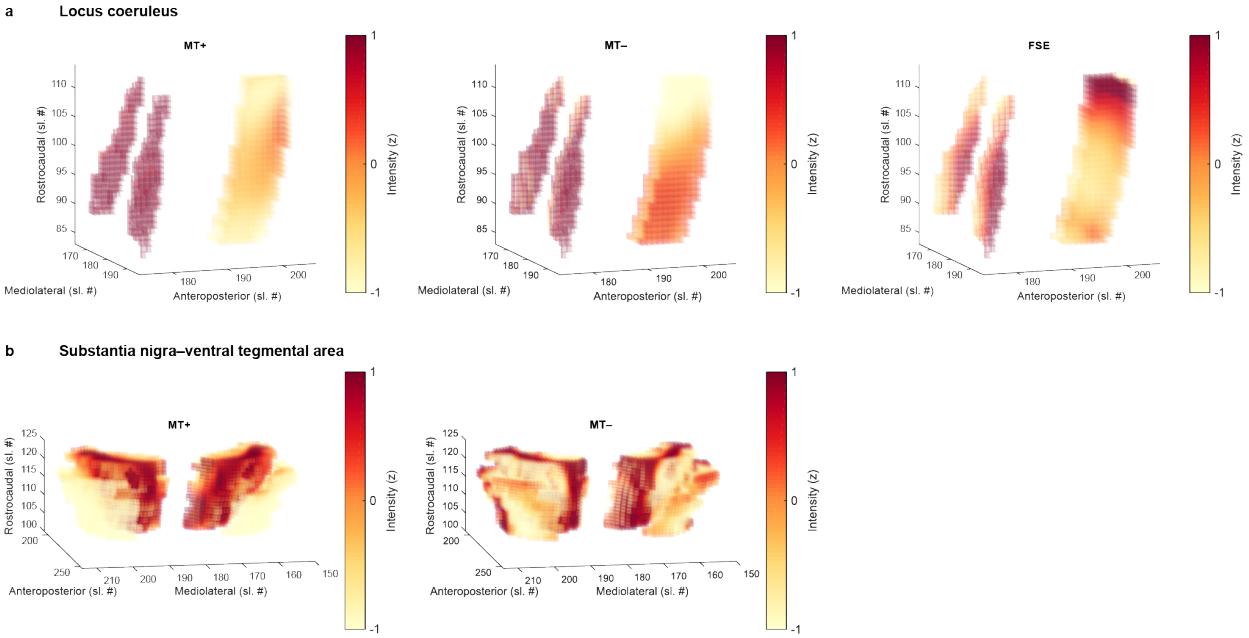

Figure 2. Normalized intensity in the LC, SN–VTA, and corresponding white-matter reference regions. Hyperintensities corresponding to the (**a**) LC and (**b**) SN–VTA are evident in group templates based on a Fast Spin Echo (FSE) sequence, and a Magnetization Transfer sequence, acquired once with a dedicated magnetic saturation pulse (MT+) and once without, resulting in a proton density image (MT–). LC and reference volumes of interest are taken from [68], SN–VTA and reference volumes of interest are based on [58]. The reference regions are located anterior of the LC and SN–VTA, respectively. In the visualization, they can be seen as rectangular shape to the right of the LC (i.e., the two red columns) as well as in front of the SN–VTA (i.e., the red curved shape). Note that our FSE sequence only covered the brainstem. Templates were estimated across age groups. LC, locus coeruleus; SN–VTA, substantia nigra–ventral tegmental area.

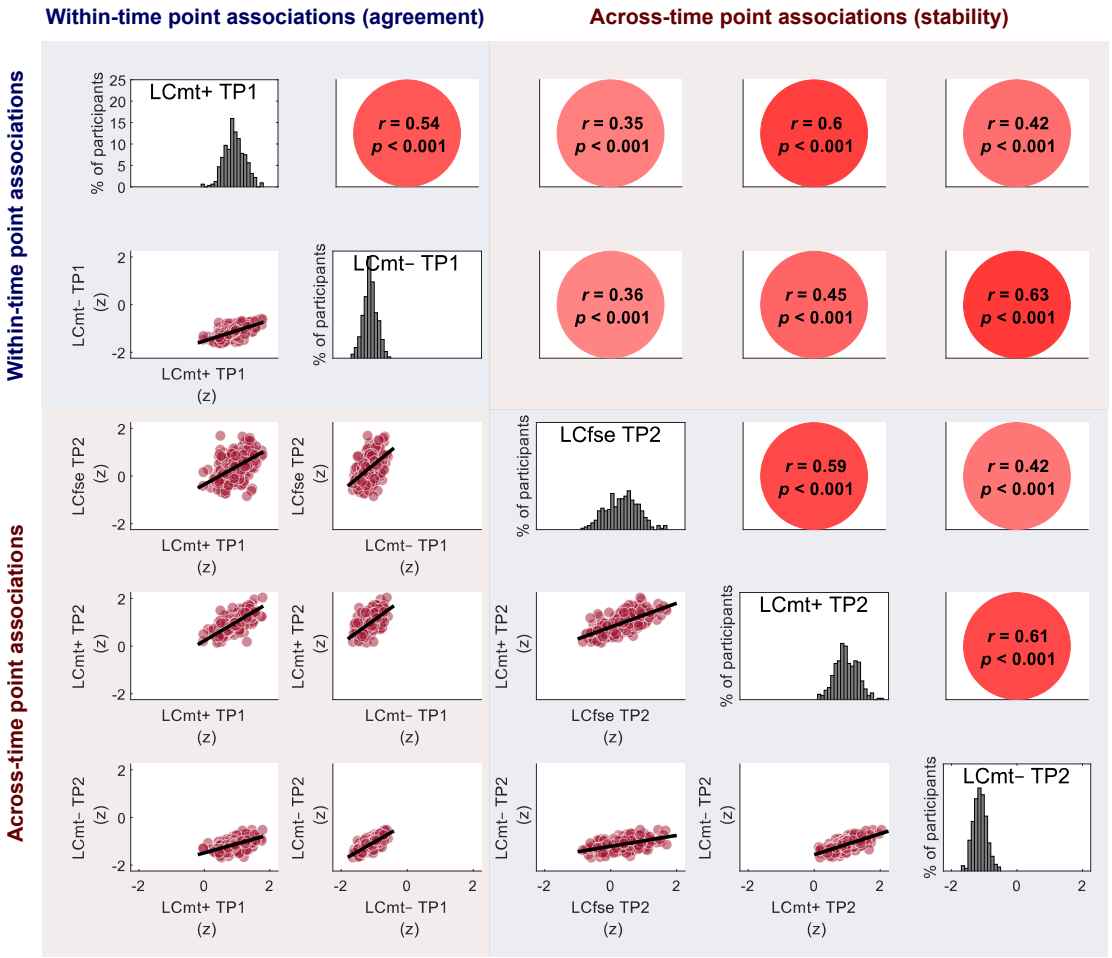

Figure 3. Younger and older adults' LC intensities are correlated across imaging modalities—a marker for their agreement—and across time points—a marker for their stability. Visualized data are based on the statistical model depicted in Figure S14. For the same analyses using SN–VTA data, see Figures S18 and S20. Note, the diagonal shows LC intensity, standardized across all sequences and time points, to facilitate comparing intensity distributions. Imaging sequences included a Fast Spin Echo (FSE) sequence, and a Magnetization Transfer sequence, acquired once with a dedicated magnetic saturation pulse (MT+) and once without, yielding a proton density image (MT–). LC, locus coeruleus; TP, time point; SN–VTA, substantia nigra–ventral tegmental area.

Multimodal locus coeruleus and substantia nigra–ventral tegmental area integrity factors show high stability over time

Making use of the longitudinal nature of this dataset, we next explored the stability of our integrity estimates over time (TP1–TP2; mean delay ~1.9 (SD 0.7) years), as a proxy for their reliability [95]. Longitudinal studies investigating the reliability of imaging sequences for catecholaminergic nuclei are sparse. Thus, as a reference, we first assessed the stability of the modality-specific intensity factors and found evidence for an intermediate stability, for younger and older adults' LC: MT+, $r = 0.6$; $p < 0.001$; MT–, $r = 0.63$; $p < 0.001$; for younger and older adults' SN–VTA: MT+, $r = 0.66$; $p < 0.001$; MT–, $r = 0.18$; $p = 0.17$ (see Figures 3 and S14, S18, S20; FSE sequence only available for TP2 [see Methods]). For comparable analyses using intensity values extracted from the pontine reference (LC) and crus cerebri reference (SN–VTA) regions, see Figures S23 and S24.

If our multimodal integrity factors remove modality-specific measurement error [85], we should observe a higher stability across time points for the multimodal as compared to the modality-specific factors. Importantly, our multimodal LC and SN–VTA factors indeed evinced a higher stability, pointing to the benefits of the multimodal imaging approach, $r = 0.88$; $p < 0.001$ for younger and older adults' LC (test against mean modality-specific stability [i.e., $r = 0.615$], $z = 11.713$, $p < 0.001$); $r = 0.67$; $p < 0.001$ for younger and older adults' SN–VTA (test against mean modality-specific stability [i.e., $r = 0.448$], $z = 5.837$; $p < 0.001$) [96].

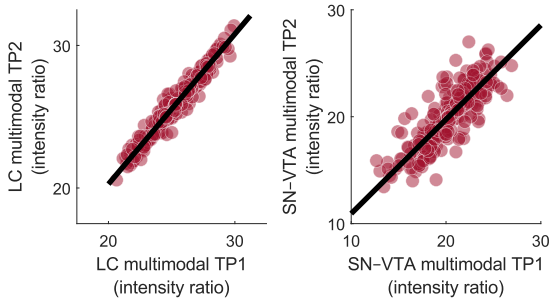

Figure 4. Multimodal LC and SN–VTA estimates show high stability over time points (mean delay ~ 1.9 years), $r = 0.88$; $p < 0.001$ for younger and older adults' LC (test against mean modality-specific stability, i.e., $r = 0.615$, $z = 11.713$; $p < 0.001$); $r = 0.67$; $p < 0.001$ for younger and older adults' SN–VTA (test against mean modality-specific stability [i.e., $r = 0.448$], $z = 5.837$; $p < 0.001$). LC, locus coeruleus; SN–VTA, substantia nigra–ventral tegmental area.

Locus coeruleus and substantia nigra–ventral tegmental area are associated with different aspects of late-life memory performance

Next, we cross-sectionally probed the behavioral implications of interindividual differences in LC and SN–VTA integrity, using data of TP2. For this, we leveraged a comprehensive cognitive battery and a previously established factor structure [86] to aggregate performance across several working memory, episodic memory, and fluid intelligence tasks and capture their shared variance on a latent level (see Figure S9). We observed strong age differences in each of the cognitive domains (see Figure 5), older relative to younger adults (mean age difference [standard error]): working memory, –2.265 (0.309); episodic memory, –2.287 (0.309); fluid intelligence, –2.073 (0.295); all $p < 0.001$. Importantly, however, when we added estimates for the catecholaminergic nuclei to the model, we found that higher LC and SN–VTA integrity were related to better performance (i.e., less age-related cognitive impairments) across domains, $\Delta\chi^2(df = 3) = 25.11$; $p < 0.001$ for older adults' LC; $\Delta\chi^2(df = 3) = 7.86$; $p = 0.049$ for older adults' SN–VTA (see Figure S10).

Dopaminergic and noradrenergic neuromodulatory centers are densely interconnected [38,97]. In addition, dopamine is the biosynthetic precursor of noradrenaline [45], and indeed we detected a positive association between the structural metrics of the two neuromodulatory nuclei, $r = 0.25$; $\Delta\chi^2(df = 1) = 5.75$; $p = 0.017$ for older adults (cf. Figure 6 and see S10). However, while the LC and SN–VTA were positively coupled, they, differed in their association with late-life cognition, $\Delta\chi^2(df = 3) = 15.66$; $p = 0.001$ for older adults.

Follow-up analyses showed that higher LC integrity was related to better episodic memory performance, $r = 0.49$; $\Delta\chi^2(df = 1) = 21.44$; $p < 0.001$ for older adults (cf. Figure 6 and see S10) and that this association was specific: That is, LC's relation to cognition differed across domains (episodic memory, working memory, and fluid intelligence), $\Delta\chi^2(df = 2) = 10.64$; $p = 0.005$ for older adults. Moreover, the LC–episodic memory association was stronger than that of the SN–VTA and episodic memory, $\Delta\chi^2(df = 1) = 6.63$; $p = 0.01$ for older adults. Taken together, our findings show a general (i.e., task and imaging sequence independent), yet specific relation of LC and late-life episodic memory performance, corroborating and extending earlier work [68,69,88,98,99].

In contrast to the LC, higher SN–VTA integrity correlated with better late-life working memory, $r = 0.28$; $\Delta\chi^2(df = 1) = 6.76$; $p = 0.009$ for older adults (cf. Figure 6 and see S10). There was a numerical tendency for differential associations of SN–VTA integrity with performance in each of the cognitive domains (working memory, episodic memory, and fluid intelligence), $\Delta\chi^2(df = 2) = 5.73$; $p = 0.057$ for older adults. However, we did not observe reliable differences in the relation of the two neuromodulatory nuclei to working memory, $\Delta\chi^2(df = 1) = 2.01$; $p = 0.156$ for older adults. In sum, our findings suggest a differential association of the two neuromodulatory systems with late-life memory performance. While episodic memory was associated with LC integrity, SN–VTA integrity was related to working memory.

Note that our model (see Figure S10) specified correlations between the latent catecholaminergic and cognitive factors. That is, it probed associations of one neuromodulatory system with cognition irrespective of the other neuromodulatory system. Thus, we additionally specified a second, statistically equivalent model in which we searched for unique associations with cognition for each catecholaminergic system while controlling for the respective other system, using a multiple regression approach (see [85] for a comparable approach; see Figure 6 and S11). Crucially, we again detected reliable LC–episodic memory, $\beta = 0.5$; $\Delta\chi^2(df = 1) = 19.55$; $p < 0.001$, and SN–VTA–working memory associations, $\beta = 0.28$; $\Delta\chi^2(df = 1) = 6.05$; $p = 0.014$, for older adults, underlining differential relations to cognition of the two neuromodulatory nuclei.

Younger and older adults showed comparable associations between neuromodulatory integrity and memory performance (test for age group differences in (1) the LC–episodic memory association: ($\Delta\chi^2$(df = 1) = 0.43; p = 0.512; and (2) the SN–VTA–working memory association: $\Delta\chi^2$(df = 1) = 0.28; p = 0.594). Model visualizations, model fit, and younger adults' findings are reported in the supplementary information (see Figures S10 and S11 and [94]).

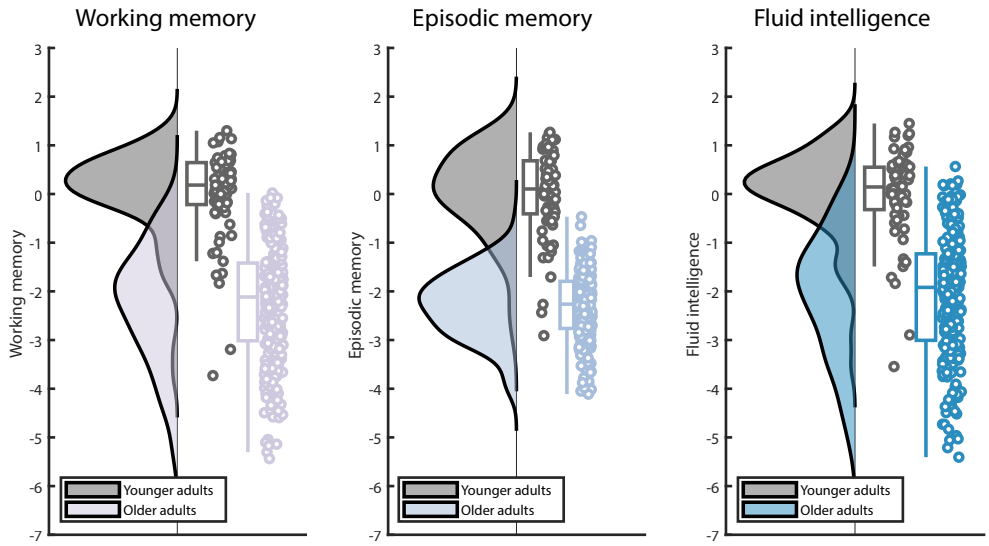

Figure 5. Cross-sectional age differences in working memory, episodic memory, and fluid intelligence factors at TP2 (for the statistical model, see Figure S9). Older adults show lower performance relative to younger adults across cognitive domains (mean age difference [standard error]): working memory, –2.265 (0.309); episodic memory, –2.287 (0.309); fluid intelligence, –2.073 (0.295); all $p < 0.001$. Raincloud plots based on [100]. For visualizations of episodic memory and working memory performance over time points 1–3, see Figure S27–28.

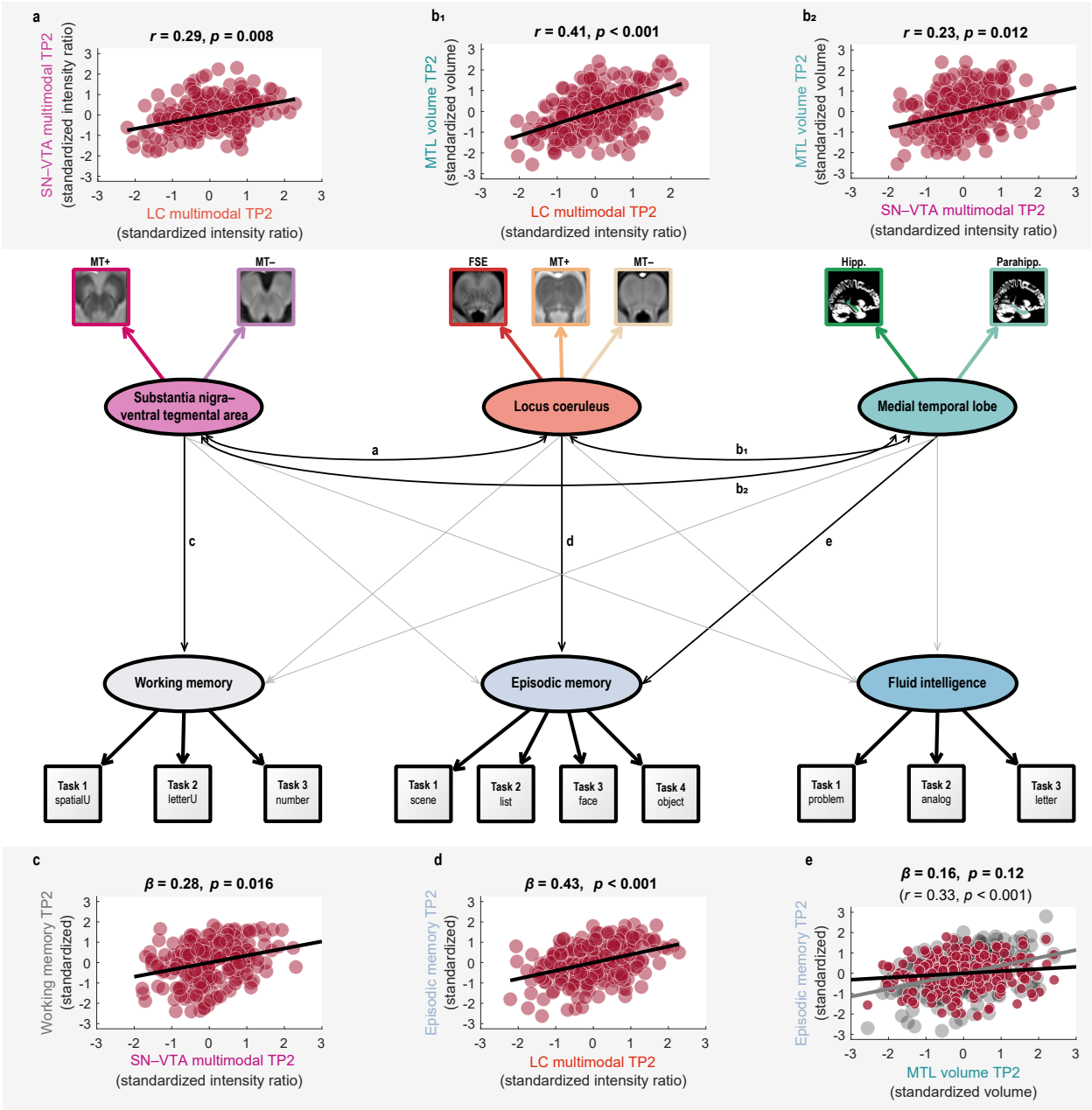

Figure 6. Schematic pictorial rendition of a structural equation model probing the interrelation of catecholaminergic nuclei and medial temporal lobe volume (paths **a** and **b**) and their unique associations with late-life cognition (paths **c**–**e**) in older adults at TP2. Note that covariances among cognitive factors, intercepts, and error terms are omitted for clarity. For the full statistical model, see Figure S13. Task*, cognitive paradigm (indicator; [square]) for the respective cognitive domain (latent factor; [ellipse]); One-headed arrows, regression; Double-headed arrow, correlation. Note that the brightness of paths indicates their significance. Medial temporal lobe volumes only demonstrate a reliable association with episodic memory in a correlational model (see grey line in scatter plot **e**; cf. Figure S12), but not when controlling for catecholaminergic neuromodulation (see black line in scatter plot **e**). Locus coeruleus (LC) and substantia nigra–ventral tegmental area (SN–VTA) factors are derived from a Fast Spin Echo (FSE) sequence, and a Magnetization Transfer sequence, acquired once with a dedicated magnetic saturation pulse (MT+) and once without, resulting in a proton density image (MT–). Hipp, hippocampus volume; Parahipp, parahippocampus volume.

Locus coeruleus and substantia nigra–ventral tegmental area are associated with memory performance over and above medial temporal lobe volumes

Via direct projections, the LC and SN–VTA release catecholamines in memory-relevant brain regions, such as the medial temporal lobe [42,44,47], which improves retention performance [36,38,42,44,46,47]. Abnormally phosphorylated tau, an indicator of neurodegenerative diseases such as Alzheimer's, starts to accumulate early in life in catecholaminergic nuclei [13,101–103]. With advancing age, abnormal tau also appears in projection targets of the neuromodulatory nuclei, like the medial temporal lobe [13,102,104,105], which may facilitate degeneration [68,69,105,106]. Thus, as a control analysis, we also incorporated medial temporal lobe volumes in our models linking catecholaminergic nuclei and cognition (see Figure S12 and S13).

In a correlational model, we observed that the integrity of both catecholaminergic nuclei was positively associated with medial temporal lobe volumes, $r = 0.41$; $\Delta\chi^2(df = 1) = 27.45$; $p < 0.001$ for older adults' LC; $r = 0.23$; $\Delta\chi^2(df = 1) = 6.29$; $p = 0.012$ for older adults' SN–VTA (cf. Figure 6 and see S12), potentially indicating neuroprotective catecholaminergic effects [107,108]. In addition, higher medial temporal lobe volumes were related to better late-life episodic memory performance, $r = 0.33$; $\Delta\chi^2(df = 1) = 14.22$; $p < 0.001$ for older adults, in line with its role in memory processing [109].

Importantly, when we specified a second, multiple-regression model that searches for unique effects, we found that the LC was still reliably associated with episodic memory performance, $\beta = 0.43$; $\Delta\chi^2(df = 1) = 11.96$; $p < 0.001$ for older adults, while medial temporal lobe volumes were not, $\beta = 0.16$; $\Delta\chi^2(df = 1) = 2.46$; $p = 0.117$ for older adults (see Figure 6 and S13), when accounting for the respective other regions (e.g., controlling for SN–VTA and medial temporal lobe volume when evaluating the association between LC and episodic memory). Similarly, the SN–VTA was related to working memory after controlling for medial temporal lobe volumes and LC integrity, $\beta = 0.28$; $\Delta\chi^2(df = 1) = 5.8$; $p = 0.016$ for older adults. For comparable analyses that are based on intensity values averaged across the LC or SN–VTA, see Table S 5.

Taken together, our results suggest a robust association of catecholaminergic nuclei and memory that cannot be fully accounted for by medial temporal lobe volume.

Longitudinal changes in locus coeruleus integrity predict future episodic memory performance

Cross-sectional studies point to late-life differences in catecholaminergic nuclei [69,75–77,88,110], however, longitudinal data showing within-person changes are scarce. Thus, we combined imaging data of the two time points (TP1–TP2; mean delay ~1.9 years) to test for individual changes in LC and SN–VTA integrity estimates in later life [87,111].

First, we observed that change in the catecholaminergic nuclei was correlated across imaging modalities (MT+, MT–; no longitudinal FSE data available), suggesting that the different MR sequences pick up a common underlying construct (i.e., change in catecholaminergic nuclei), $r = 0.16$; $\Delta\chi^2(df = 1) = 6.09$; $p = 0.014$ for older adults' LC; $r = 0.13$; $\Delta\chi^2(df = 1) = 5.91$; $p = 0.015$ for older adults' SN–VTA (see Figure S16 and S21). Thus, we again integrated across sequences to retrieve multimodal latent change factors for LC and SN–VTA integrity (see Figure S17 and S22). For both catecholaminergic systems, we found reliable individual differences in change, $\Delta\chi^2(df = 1) = 6.09$; $p = 0.014$ for older adults' LC; $\Delta\chi^2(df = 1) = 5.91$; $p = 0.015$ for older adults' SN–VTA. However, there was no reliable mean change at the group level in either nucleus, ps > 0.1 in older adults. That is, we observed that older adults differed from one

another in how their LC and SN–VTA changed over time—while some older adults showed increases in intensity ratios, others showed decreases (see Figure 7; cf. [69,75]). Control analyses indicated, that changes in neuromodulatory integrity were not associated with the spatial positions from which intensity ratios were sampled at time point 1 and 2, making movement in the scanner an unlikely explanation for individual differences in change (see Figure S32).

Finally, to test the behavioral implications of these late-life changes in catecholaminergic nuclei, we probed whether our neural change model (TP1–TP2) could be used to predict future cognition (at TP3; using the previously established cognitive factor structure, cf. Figure S9). We additionally included chronological age (at TP2) as a predictor, to test and account for potential age effects in rate of decline (see Figure S29 and S30).

Note that we here related changes in catecholaminergic nuclei to subsequent cognitive performance (at TP 3), as our analyses indicated task-specific memory changes (see methods and supplementary results).

In line with a late-life degeneration of neuromodulatory centers [7,10,11,69], we found more negative change in the LC and SN–VTA with increasing age, $\beta = -0.18$; $\Delta\chi^2(df = 1) = 4.81$; $p = 0.028$ for older adults' LC; $\beta = -0.29$; $\Delta\chi^2(df = 1) = 3.95$; $p = 0.047$ for older adults' SN–VTA. Moreover, we observed that changes in LC integrity predicted subsequent episodic memory performance over and above chronological age, $\beta = 0.23$; $\Delta\chi^2(df = 1) = 4.73$; $p = 0.03$ for older adults' LC (see Figure 7); $\beta = 0.27$; $\Delta\chi^2(df = 1) = 1.55$; $p = 0.213$ for older adults' SN–VTA (see Figure S31). Taken together, our results are in line with the proposition that a decline of the LC in later life is associated with diminished episodic memory performance [10,69,88,112].

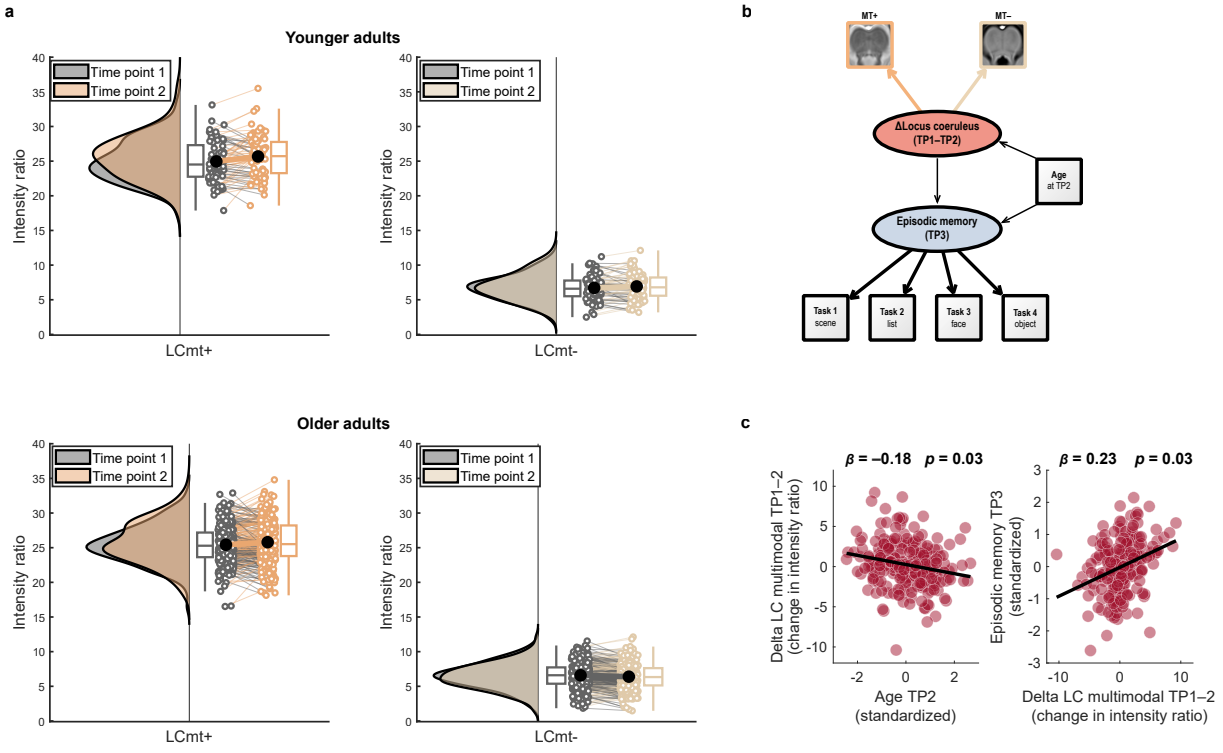

Figure 7. Longitudinal changes in LC intensity ratios and their association with age and future memory performance in older adults. **a**, Numerically, older adults show more negative average change in LC intensity across time points

as compared to younger adults. MRI sequences include a Magnetization Transfer sequence, acquired once with a dedicated magnetic saturation pulse (MT+) and once without, resulting in a proton density image (MT–). For the Fast Spin Echo-sequence, only cross-sectional data are available. **b,** Schematic depiction of the structural equation model probing the association of longitudinal change in multimodal LC integrity with future episodic memory performance, accounting for chronological age. For the full model, see Figure S29. **c**, Scatter plots showing (1) more negative LC change in older adults of higher age and (2) a prediction of future memory performance based on LC change (controlling for chronological age). For comparable analyses using SN–VTA and working memory data, see Figures S30 and S31. Raincloud plots based on [100]. LC, locus coeruleus; SN–VTA, substantia nigra–ventral tegmental area.

Discussion:

This study sought to disentangle the effects of declining dopaminergic and noradrenergic neuromodulation on late-life memory. We took advantage of a multimodal imaging protocol and extensive cognitive assessments across several time points to contrast the behavioral implications of LC and SN–VTA integrity.

Our findings indicate that different imaging approaches for catecholaminergic nuclei (FSE, MT+, MT–) show a high agreement. Thus, we used latent-variable modeling to integrate across MRI modalities and retrieve multimodal LC and SN–VTA integrity factors that demonstrated a markedly increased reliability compared with their individual components. After establishing reliable in-vivo integrity proxies, we probed their associations with late-life cognition. We used an extensive neuropsychological test battery and a previously identified factor structure to demonstrate that these two catecholaminergic systems, although positively coupled, differ in their relationship three domains of aging cognition: episodic memory, working memory, and fluid intelligence.

We observed a general (i.e., task and imaging sequence independent), yet specific association of LC integrity and late-life episodic memory performance (i.e., stronger for episodic memory as compared to working memory and fluid intelligence). By contrast, SN–VTA integrity was linked to better working memory. Remarkably, both associations remained reliable even after accounting for the respective other neuromodulatory system and a key node in the memory network, the medial temporal lobe, suggesting robust effects. Corroborating this interpretation, associations between catecholaminergic integrity and late-life memory performance were qualitatively unchanged when including participants' age, education, and sex as covariates (see *Supplementary results*).

Leveraging the longitudinal nature of this dataset, we also investigated late-life changes in the LC and SN–VTA over a delay of approximately two years. A principal finding was that older age was associated with more negative change in each catecholaminergic system, in line with the late-life degeneration of neuromodulatory centers. Moreover, we showed that changes in the LC predicted future episodic memory performance over and above chronological age and education (see *Supplementary results*). Taken together, this study suggests dopaminergic and noradrenergic neuromodulation play domain-specific roles in determining the trajectory of cognition in later life and provides novel insights into the neural basis of human senescent memory decline.

The loss of dopaminergic neuromodulation has long been recognized as crucial determinant of late-life cognitive deficits [7–9]. More recently, technical advances have also facilitated studies of the noradrenergic LC [56] that long seemed unattainable [52,53]. We used two types of imaging sequences (FSE, MT+) validated on postmortem specimen of the LC [57] and SN–VTA [58,59]. Neuromelanin, an insoluble catecholamine-derived pigment that traps metals and exhibits paramagnetic properties, is thought to contribute to the hyperintensity of catecholaminergic nuclei [17,56,58,59,62,63]. Moreover, the high density of water protons and paramagnetic ions in large catecholaminergic neurons has also been proposed as source of their MRI contrast [65,66]. In line with this, we provide the first quantification of the LC and SN–VTA based on a proton density-weighted sequence (i.e., without dedicated magnetization transfer preparation pulse; MT–). Magnetization transfer imaging studies frequently estimate a ratio score based on sequences with and without dedicated preparation pulse (i.e., MT+ and MT–) [113]. However, the sensitivity of our MT– sequence for the LC and SN–VTA suggests that this ratio would reduce the detectability of these nuclei. Notably, we observed that despite differences in mean contrast, LC and SN–VTA hyperintensities were correlated across all imaging modalities (FSE, MT+, MT–), suggesting that they provide convergent information about the same underlying construct (i.e., catecholaminergic nuclei).

397 We thus leveraged our multimodal approach to estimate latent factors for catecholaminergic nuclei
398 integrity based on the commonalities across imaging sequences while removing modality-specific
399 measurement error [84,85]. Moreover, using data from both imaging time points, we show that
400 semiautomatic analyses of the intensity of catecholaminergic nuclei have high reliability, especially when
401 multimodal assessments are available [114].
402 The retention of salient experiences is enhanced by catecholamine release in the hippocampus which
403 facilitates synaptic plasticity and memory [36,38,47]. While the SN–VTA has long been attributed as
404 source of the memory-enhancing dopaminergic inputs [36,39,44], recent findings point to a denser
405 innervation by the LC that can provide noradrenergic as well as dopaminergic signals [42,46,47]. Here we
406 compared the association of the two catecholaminergic centers with an extensive set of tasks that are
407 thought to depend more (episodic memory) or less (working memory) on hippocampal processing
408 [109,115]. We observed that LC integrity was specifically related to late-life episodic memory
409 performance (as compared to working memory or fluid intelligence) and that this association was stronger
410 than the SN–VTA–episodic memory relationship. While we observed comparable associations between
411 neuromodulatory integrity and memory performance when comparing age groups, the lower sample size
412 for younger adults [57] may have limited our ability to detect effects in this group alone. Mechanistically,
413 our finding of an LC–episodic memory association might be explained by a catecholaminergic
414 modulation of hippocampal synaptic plasticity [42,46,47], but our data cannot rule out other memory-
415 related mechanisms, such as gain modulation [8,24–27] and prefrontal delay activity [12,30]. Our
416 observations are supported by a series of large-scale in-vivo imaging studies that showed reliable LC–
417 cognition associations in aging [69,88,98,99], and particularly with episodic memory [69,88,116]. In
418 addition, they concord with a recent report linking anteromedial and superior substantia nigra intensity to
419 attentional performance [117], a cognitive concept overlapping with working memory [25].
420 Animal research suggests also a noradrenergic role in attentional processes [12,25,118], particularly in
421 tasks that require attentional re-orienting [119,120]. By contrast, the working memory indicator tasks used
422 in the current study (e.g., number n-back) require participants to hold information active in mind and may
423 thus depend less on noradrenergic neuromodulation (but see [32]). Interestingly, time-resolved measures
424 associated with phasic locus coeruleus activity (pupil dilation, P-300 event-related potential [26,121–
425 123]) show consistent associations with individual differences in attentional performance [124,125],
426 calling for more multimodal research.
427 Cross-sectional studies point to late-life differences in catecholaminergic nuclei [75–77,88,110]. Here we
428 provide the first characterization of late-life longitudinal changes in the LC and SN–VTA. In general
429 agreement with extrapolations from cross-sectional data, we found more negative change in both
430 catecholaminergic systems with increasing age. Subcortical neuromodulatory centers like the LC and the
431 SN–VTA are among the first sites to accumulate pathology in age-associated diseases like Alzheimer's
432 [13] and Parkinson's [73], and show severe degeneration with disease progression [16,126]. In
433 combination with earlier work suggesting lower catecholaminergic contrast with advancing age might be
434 linked to impending pathology [68,71,78,79,117], our findings may indicate subthreshold pathological
435 processes in a subset of our older participants. This interpretation is supported by our prediction of poorer
436 future memory performance in individuals with more negative LC change [112]. Accordingly, recent
437 meta-analyses demonstrate the efficacy of noradrenergic treatments in improving cognitive symptoms in
438 Alzheimer's disease [127]. Mirroring its clinical potential, MRI-indexed catecholaminergic integrity has
439 been suggested as useful tool for stratifying patients suffering for neurodegenerative diseases in clinical
440 trials that include noradrenergic treatments [56,128]. A subset of older participants also showed LC and

441 SN–VTA intensity increases over time, which might indicate higher intracellular proton density [66],
442 potentially linked to the activity-related volume increase of catecholaminergic cells [11,15,129,130].
443 The present study highlights the utility of multimodal longitudinal assessments of catecholaminergic
444 nuclei to elucidate the neurobiological basis of senescent memory decline. We dissociated the roles of the
445 noradrenergic LC and dopaminergic SN–VTA in late life cognition. While the former showed robust
446 associations with current and future episodic memory performance, the latter showed a relationship to
447 better working memory performance. These findings point to differential roles of dopaminergic and
448 noradrenergic neuromodulation in late-life cognition with potential implications for age-associated
449 diseases like Alzheimer's and Parkinson's [13,69,73]. Accurate longitudinal assessments of
450 catecholaminergic nuclei may constitute promising early markers for predicting cognitive decline in later
451 life.
452

453 **Methods:**

454 Study design and participants:

455 Data were collected as part of the Berlin Aging Study-II (BASE-II), an ongoing longitudinal study that
456 investigates neural, cognitive, physical, and social conditions related to successful aging (for more
457 information, see https://www.base2.mpg.de/en , references [80–83], and the supplementary methods).
458 Cognitive performance was assessed in three time periods (TP1–TP3) between 2013 and 2020 (TP1:
459 2013–2015; TP2: 2015–2016; TP3: 2018–2020) with a mean duration between cognitive assessments of
460 2.246 years (TP1–2; SD: 0.603) and 2.917 years (TP2–TP3; SD: 0.438).
461 A subset of BASE-II participants also underwent magnetic resonance imaging (MRI). Eligible
462 participants had no history of neurological or psychiatric disorders, or head injuries, and did not take
463 medication that may affect memory function. Imaging data were collected in two time periods (TP1, TP2)
464 in temporal proximity to the cognitive assessments (mean delay between MRI waves 1.894 years; SD:
465 0.656). Participants were only considered for further analyses if at least one type of imaging sequence
466 sensitive for dopaminergic or noradrenergic neuromodulatory centers was available (see below). For TP1,
467 this corresponds to 288 participants out of a total of 488 participants with imaging data, whereas for TP2
468 this corresponds to 320 out of 323 participants with imaging data. Thus, our analyses included a total of
469 320 individual participants. While not all imaging sequences were available for all participants (see Table
470 1), 203 participants have relevant MRI data for both TP1 and TP2.
471 The final sample (n = 320) included 69 younger adults (22 female; mean age (SD): 32.705 (3.884) years
472 [at TP2]) and 251 older adults (91 female; mean age (SD): 72.414 (4.045) years [at TP2]). Sample
473 descriptives are reported in Table 2.
474 The cognitive and imaging assessments were approved by the institutional review boards of the Max
475 Planck Institute for Human Development and the German Psychological Society (DGPS), respectively.
476 Participants provided written informed consent and were reimbursed for their participation.
477

Table 1: Overview of participants with available imaging data

Magnetic resonance imaging sequence	Time period	Number of participants with relevant imaging data	Total number of participants with imaging data
Magnetization Transfer (MT+) *and* Proton Density (MT–)	1	288	448
Magnetization Transfer (MT+) *and* Proton Density (MT–)	2	260	323
Fast Spin Echo (FSE)	1	0	448
Fast Spin Echo (FSE)	2	316	323
Fast Spin Echo (FSE) *and* Magnetization Transfer (MT+) *and* Proton Density (MT–)	1	0	448
Fast Spin Echo (FSE) *or* Magnetization Transfer (MT+) *and* Proton Density (MT–)	1	288	448
Fast Spin Echo (FSE) *and* Magnetization Transfer (MT+) *and* Proton Density (MT–)	2	256	323
Fast Spin Echo (FSE) *or* Magnetization Transfer (MT+) *and* Proton Density (MT–)	2	320	323

Note: Relevant imaging data refers to participants with a whole-brain T_1-weighted (MPRAGE) sequence as well as a sequence sensitive for dopaminergic or noradrenergic neuromodulatory centers (Magnetization Transfer (MT+), Proton Density (MT–) or Fast Spin Echo (FSE)). By contrast, the total number of participants with imaging data reflects all participants that underwent MRI, irrespective of sequence type. The Magnetization Transfer and Proton Density sequences were acquired in succession in each scan session (i.e., identical sequence, acquired once with and one without dedicated MT preparation pulse). Thus, they are grouped in the table.

487 **Table 2:** Summary of sample descriptives for younger and older adults

	Younger adults (n = 69; 22 female)		Older adults (n = 251; 91 female)	
	Mean (SD)	Range	Mean (SD)	Range
Age (years; at time period 2)	32.705 (3.884)	25.414–40.203	72.414 (4.045)	62.534–83.162
Education (years) (available for n = 285)	14.242 (2.519)	10–18	14.08 (2.924)	7–18
Mini Mental State Examination (available for n = 204)	–	–	28.613 (1.336)	24–30

488 *Note*: Mini Mental State data was assessed around TP3, during a medical examination at a different visit
489 as part of the longitudinal Berlin Aging Study-II. *SD,* Standard Deviation.

490

Cognitive data assessment:

At TP1–TP3, cognition was tested using a comprehensive computerized battery probing key cognitive functions. Performance was assessed in small groups of four to six participants. Cognitive test sessions lasted approximately 3.7 h and included 16 tasks (at TP2), of these, three measured working memory, four episodic memory, and three fluid intelligence [131]. While the exact composition of the cognitive assessments changed across waves, the same tasks were used to measure working memory, episodic memory and fluid intelligence at TP1–TP3. Only older adults were tested at TP3. For a detailed task description, please refer to [131–133], below we provide a brief overview of the measures relevant to the current analyses.

Working memory assessment:

Spatial Updating (abbreviated as *spatial-u*): Participants were shown a display of two to three 3 × 3 grids, in each of which a blue dot was presented in one of the nine tiles. Participants were asked to memorize the locations of the blue dots and mentally update them according to shifting operations that were indicated by arrows appearing below the dots. Six updating operations were required before the 3 × 3 grids reappeared and participants indicated the end position of the blue dots (by mentally combining their start position and the six shifting operations). We used the number of correct placements as an indicator of working memory performance [131,133].

Letter Updating (abbreviated as *letter-u*): Participants were shown a sequence of 7–13 letters. Once the presentation ended, they were asked to report, in correct order, the last three letters that were shown. The number of correctly reported letters was used as a measure of working memory performance [131].

Number N-back (abbreviated as *number*): Three digits (1–9) were presented consecutively in three adjacent cells, followed by the next sequence of three digits. Participants indicated by button press whether the currently presented digit matched the digit shown three steps before [131,133]. We took participants' accuracy as indicator of their working memory performance.

Episodic memory assessment:

Scene encoding (abbreviated as *scene*): Participants incidentally encoded 88 scene images by performing indoor/outdoor judgments on each image. The encoding phase was followed by an old/new recognition memory test, which included confidence judgments. Recognition memory was tested after a delay of approximately 2.5 hours and served as episodic memory performance index (hits – false alarms) [85,88,131].

Verbal learning and memory task (abbreviated as *list*): Participants first learned a 15-word list that was presented via headphones. The task was composed of five learning trials each followed by a free recall period in which participants entered the words they remembered via keyboard (trial 1–5; recall of learning list). After these initial learning–recall cycles, participants were presented an interference list and their delayed recall and recognition memory was assessed. The sum of correctly recalled words during the learning–recall cycles (trial 1–5) served as episodic memory measure [85,88,131].

Face–profession task (abbreviated as *face*): Participants studied 45 pairs of face images and profession words. The tasks consisted of an incidental encoding phase, a 2-minute distraction phase, and finally a recognition memory task including old, new as well as rearranged face–profession pairs. Corrected recognition memory scores for rearranged pairs was used as the performance index.

Object–location task (abbreviated as *object*): Participants encoded the location of 12 digital photographs of real life objects on a 6 × 6 grid. After encoding, the objects reappeared next to the grid and participants were instructed to reproduce their correct location by placing the items in the grid. The sum of correct placements served as index of episodic memory.

Fluid intelligence assessment:

Practical problems (abbreviated as *problem*): Participants were sequentially presented eighteen items depicting everyday problems (e.g., the hours of a bus timetable, a subway map etc.), in order of ascending difficulty. For each of these problems, five response alternatives were provided and participants selected the correct option by clicking on it. We took the sum of correctly solved problems as measure of fluid intelligence [131,134].

Figural analogies (abbreviated as *analog*): Participants were instructed to draw analogies. They were presented with twenty-two items in ascending difficulty that followed the format *A* is to *B* as *C* is to *X*? Below each item, five response alternatives were presented and participants selected the correct option by clicking on it. The sum of correctly given answers served as index of fluid intelligence [131,134].

Letter series (abbreviated as *letter*): Participants were shown twenty-two series of five letters, each ending with a question mark (e.g., c-e-g-i-k-?). Each series followed a simple rule (e.g., +1, –1, +2; or +2, –1), with increasing difficulty. Below each letter series, five response alternatives were presented and participants selected the correct option by clicking on it. The sum of correct responses served as fluid intelligence measure [131,134].

All tasks included practice blocks to familiarize participants with the instructions. Note that these tasks have previously been used to estimate latent factors of working memory, episodic memory, and fluid intelligence [131] (also see [85,88,135]).

562 Magnetic resonance imaging data assessment:

563 To investigate the associations of dopaminergic and noradrenergic integrity with late-life cognition,
564 younger and older participants underwent 3T-MRI at TP1 and TP2 (MAGNETOM TIM Trio, Siemens
565 Healthcare). Only those sequences used in the current analyses are described below. The imaging protocol
566 included three scans sensitive for the SN–VTA and LC—a Fast Spin Echo sequence (FSE; sometimes
567 also called Turbo Spin Echo [TSE]), and a Magnetization Transfer sequence, acquired once with a
568 dedicated magnetic saturation pulse (MT+) and once without, resulting in a proton density image (MT–).
569 Moreover, a Magnetization Prepared Gradient-Echo (MPRAGE) sequence, comparable to the ADNI
570 protocol (www.adni-info.org), was collected to facilitate coregistration to standard space and to estimate
571 volumes for regions of interest. Moreover, the MPRAGE sequence was used during acquisition to align
572 the FSE sequence perpendicularly to the plane of a participant's brainstem. Note that for some
573 participants specific absorption rate (SAR) limits were exceeded during the FSE acquisition, as reported
574 previously [88] (also see [55,136]). Sequence parameters are reported in Table 3.
575
576 **Table 3:** Overview of magnetic resonance imaging sequences

Magnetic resonance imaging sequence	Acquisition matrix; Slices (orientation; distance factor)	Voxel size (x, y, z; mm)	Repetition time (TR; ms)	Echo time (TE; ms)	Flip angle (°)
Magnetization Transfer (MT+)[1]	192 × 256 × 48 (axial; –)	1 × 1 × 3	38	5.5	10
Proton Density (MT–)[2]	192 × 256 × 48 (axial; –)	1 × 1 × 3	38	5.5	10
Fast Spin Echo (FSE)[3]	440 × 512 10 (axial; 20 %)	0.5 × 0.5 × 2.5	600	11	120
Magnetization Prepared Gradient-Echo (MPRAGE)[4]	256 × 256 × 192 (sagittal; –)	1 × 1 × 1	2500	4.77	7

577 *Note*: All sequences were acquired with a standard 32-channel head coil.
578 [1]: Magnetization Transfer Contrast (MTC) option enabled (MT pulse: 1200 Hz off-resonance, 16 ms [110]); 3-D
579 sequence
580 [2]: Magnetization Transfer Contrast (MTC) option disabled; 3-D sequence
581 [3]: Each FSE acquisition included four online averages and yielded two brainstem images. The values extracted from
582 these images were aggregated offline. SAR limits resulted in a slight variation in the number of slices [88];
583 2-D sequence; sometimes also called Turbo Spin Echo (TSE).
584 [4]: Inversion time (TI; ms): 1100; 3-D sequence
585

586 Magnetic resonance imaging data analysis:

587 We applied a previously established semi-automatic analysis procedure to extract individual LC and SN–
588 VTA intensity values from structural imaging data (for a detailed description and validation, see [88], for
589 applications, see [89,90,137]; for an independent validation see [92]). The following procedure was
590 performed separately for TP1 and TP2 imaging data.

591 Template construction and standardization:

592 First (step 1), scans of each scan modality (MPRAGE, FSE, MT+ and MT–) were iteratively aligned
593 across participants using a template-based procedure implemented in Advanced Normalization Tools
594 [ANTs] (v. 2.3 [138,139]; *antsMultivariateTemplateConstruction,* 6 iterations, including
595 *N4BiasFieldCorrection*). A schematic visualization of the procedure is included in the supplementary
596 methods. Before template construction, MPRAGE and MT– scans were resampled to 0.5 mm isometric
597 resolution (ANTs' *ResampleImage*). Moreover, to facilitate template construction, participants' native
598 space FSE scans were aligned to their template-space MPRAGE scans (*antsRegistrationSyNQuick*) [88].
599 Native space MT+ scans were aligned to resampled MT– scans to account for potential movement effects
600 between scan acquisitions (*antsRegistrationSyNQuick*). After their alignment, MT– and MT+ scans were
601 submitted to a common multimodal template construction, while FSE and MPRAGE scans each were
602 used to generate a brainstem and whole-brain template, respectively.
603 Next (step 2), modality-specific group templates (MPRAGE, FSE, MT+ and MT–) were linearly and non-
604 linearly coregistered (*antsRegistration*) to standard space (MNI-ICBM 152 linear, 0.5 mm [140]).
605 Specifically, templates with a sensitivity for catecholaminergic nuclei (FSE, MT+, MT–) were first
606 standardized to the whole-brain MPRAGE template (using a coregistration mask). Next, the MPRAGE
607 template was coregistered to MNI space and the transformations were applied to the other templates
608 (FSE, MT+, MT–; *antsApplyTransforms*). To improve coregistration accuracy, whole-brain templates
609 (MPRGAE, MT–, MNI) were skull stripped before alignment using the FMRIB Software Library [141].
610 Finally (step 3), all transformation matrices were concatenated and applied to individual participants'
611 scans to bring them from native to MNI space in a single step (*antsApplyTransforms*).

612 Semi-automatic intensity assessment:

613 To extract the intensity values of catecholaminergic nuclei, in standard space, individual scans were
614 masked with binary volumes of interest using Statistical Parametric Mapping toolbox version 12
615 (SPM12) [142] in Matlab (MathWorks). In particular, for the LC, we applied a previously established
616 high-confidence consensus mask [68]. For the SN–VTA, we relied on a previously established mask that
617 was based on manual tracings in template space [58]. Inter-participant comparisons of arbitrality scaled
618 MRI intensity values require that intensity values are normalized within participants [56]. Thus, we also
619 masked scans (FSE, MT+, MT–) with volumes of interest in potine [68] and midbrain [58] reference
620 areas, in line with earlier research [55,58,88]. Note that the fourth ventricle, which is in close proximity to
621 the LC, appears hyperintense in our MT+ scans. Thus, to rule out that the hyperintensity of the ventricle
622 could interfer with automatized LC assessments, we generated a sample-specific ventricle volume-of-no-
623 interest (based on the MT– group template), which we removed from MT+ and MT– scans before value
624 extraction (templates and ventricle mask are available from [94]). Within the masked scans (FSE, MT+,
625 MT–), we then automatically searched for the voxel of highest intensity in the LC, SN–VTA, and

reference regions. Next, for each participant, spatially-resolved intensity ratios for the LC and SN–VTA were computed per hemisphere (left, right) on a slice-by-slice basis using the following formula [55,88]:

$$LC_{Ratio} = \frac{\max(ROI) - \max(Ref)}{\max(Ref)}$$

Where max(*ROI*) denotes the peak intensity for a given slice in the LC or SN–VTA regions of interest and max(*Ref*) indicates the peak intensity in the respective reference region. For the FSE modality, two scans were available per participant (see *Magnetic resonance imaging data assessment*) and we averaged the extracted intensity ratios within participants to obtain more stable estimates. For further analyses, for all modalities (FSE, MT+, MT–) the peak intensity ratio across the regions of interest (LC, SN–VTA) was calculated as an overall integrity measure [53,68,88]. Outlier values exceeding ± 3 standard deviations were dropped, while all other values were linearly scaled (× 100) to facilitate subsequent model estimation. Note that all analyses including LC or SN–VTA data were based on peak intensity ratios. That is, the peak intensity of catecholaminergic nuclei standardized using nearby white matter regions (not their raw intensity values). To facilitate readability, we will nonetheless use the term *intensity* in our description.

At acquisition, the FSE sequence was centered on the pons and contained fewer slices compared to the MT+ and MT– sequences. As evident in Figure 2 (a), the most rostral slices of our volume of interest (LC meta mask and reference mask) reach the edges of the brainstem template and include high intensity artifacts, which, however, are reliably excluded from analyses using the semiautomatic procedure (cf. peak detection above).

Structural equation modeling:

We used structural equation modeling (SEM) to evaluate inter- and intra-individual differences in catecholaminergic nuclei and their association with cognition using the Ωnyx software environment [143] and the lavaan R package [144]. All models used full information maximum likelihood (FIML) estimation to account for missing values. The adequacy of the reported models was evaluated using χ^2-tests (i.e., an absolute fit index), as well as two frequently reported approximate fit indices: the root mean square error of approximation (RMSEA) and the comparative fit index (CFI). RMSEA values close to or below 0.06 and CFI values close to 0.95 or greater indicate good model fit [145,146]. Unless otherwise noted, multi-group models were fit, comprising submodels for younger and older adults. For this, invariance across age groups was evaluated by a hierarchical series of likelihood-ratio tests, probing group differences in (1) factor loadings (weak invariance), (2) indicator intercepts (strong invariance), and (3) residual variances (strict invariance) [147]. In case of longitudinal models, the same criteria were applied to test invariance across time [111]. After establishing adequate model fit and invariance, the significance of parameters of interest was evaluated using likelihood-ratio tests. That is, we created two nested models—in one, the parameter of interest was freely estimated, whereas in the other model it was fixed to zero. If fixing the parameter of interest to zero resulted in a drop in model fit, as evaluated using a likelihood-ratio test comparing the two nested models, this indicated the significance of the parameter [148]. We used an alpha level of .05 for all statistical tests. Statistical results with *p*-values between 0.05 and 0.1 are described as statistical trend. All analyses are based on two-sided statistical tests and did not include corrections beyond those mentioned in the respective sections. We assumed normally distributed cognitive and neural data, based on visualizations of data distributions (cf. e.g., Figures 3 and 5). In the following, cross-sectional models refer to models that include TP2 data only, while longitudinal models

evaluate the change in parameters of interest over time (TP1–TP2 or TP1–TP3). Model code, visualizations, and output are available from [94].

Cross-sectional cognitive models:

We made use of a previously established factor structure [131] to integrate performance across several working memory, episodic memory, and fluid intelligence tasks (see *Cognitive data assessment*) and capture their shared variance on a latent level. Latent variables account for measurement error in the observed scores (cognitive tasks) and thus increase statistical power to detect true effects [87].
We added covariances between the latent working memory, episodic memory, and fluid intelligence factors, as performance across these cognitive domains had been shown to be correlated [131] (see Figure S9).

Cross-sectional neural models:

We also adapted a previously established factor structure [88] to capture LC and SN–VTA intensity on a latent level. Specifically, for each region (LC, SN–VTA) and scan modality (FSE, MT+, MT–), we used the left and right hemispheric peak intensity as observed scores to estimate a modality-specific integrity factor on a latent level. Note that our FSE sequence only covered the brainstem. Thus, we cannot obtain SN–VTA estimates for this scan modality. To test the agreement in integrity estimates across modalities (FSE, MT+, MT–), we added covariances among the modality-specific latent factors for each brain region (see Figure S3).
Using the model describe above, we found a high correspondence in the integrity estimates for each nucleus across modalities (see *Results*). Thus, in a second model, we introduced a multimodal integrity factor for the LC and SN–VTA that captures the commonalities across scan modalities while removing the modality-specific measurement error (for similar approaches and a detailed discussion, see [84,85]; see Figure S4). Finally, as dopamine and noradrenaline are products of the same biosynthesis pathway, with dopamine a direct precursor to noradrenaline [45], we evaluated the association of the multimodal LC and SN–VTA integrity factors by estimating their covariance.

Cross-sectional neuro–cognitive models:

After separately establishing models for our cognitive and neural measures that showed acceptable fit and invariance across age groups, we unified these models to probe associations between catecholaminergic nuclei and cognition [88]. In the unified neuro-cognitive model, we estimated covariances between the multimodal LC and SN–VTA integrity factors and working memory, episodic memory, and fluid intelligence (correlation model; see Figures S10 and S12). In addition, we specified a second neuro-cognitive model, in which regression paths were drawn from the latent neural to the cognitive factors (regression model; see Figures S11 and S13). The correlation model evaluates associations between the LC and cognition irrespective of those between the SN–VTA and cognition. By contrast, the regression model tests whether one region explains variance in the cognitive factors over and above the other region, thus providing complementary information [85].

Longitudinal cognitive models:

Making use of the repeated assessments of cognitive performance, we tested for late-life changes in working memory and episodic memory tasks over time (TP1–TP3). Note that cognitive data at TP3 was only available for older adults (see *Cognitive data assessment*). Thus, here we relied on single-group models that excluded younger adults. In particular, we specified a latent change score model [87,149] for each cognitive task. These latent change score models yield a latent slope factor for each task that expresses participants' performance difference between TP1 and TP3 (see Figures S25 and S26).
Next, we tested whether there is a common latent factor of working memory or episodic memory change. If changes in performance were shared across tasks (i.e., task independent) of one cognitive domain, they could be captured on a higher order latent level (cf. the latent working memory and episodic memory factors in the cross-sectional cognitive model; Figure S9). To evaluate potential associations in the changes across working memory and episodic memory tasks, we added covariances among the task-specific slope terms (see Figures S25 and S26).
Most covariances across task-specific slope terms did not reach significance (see *Supplementary results*). Thus, we did not further attempt to capture task-independent changes in working memory or episodic memory on a latent level.

Longitudinal neural models:

Assessment of across-time stability:

Our cross-sectional analyses of different MRI sequences sensitive for catecholaminergic nuclei (FSE, MT+, MT–) demonstrated a high agreement in integrity estimates across imaging modalities (see *Cross-sectional neural models* and *Results* Figure 3). Leveraging the longitudinal nature of this study, we additionally explored the stability of the modality-specific integrity estimates over time (TP1, TP2), as a proxy for their reliability [95]. Specifically, we started with a modality-specific SN–VTA and LC models for TP2 (see *Cross-sectional neural models* and Figure S3) and then appended the same variables for TP1. We introduced covariances linking modality-specific factors of TP1 and TP2 to evaluate the stability in integrity estimates over time (see Figures S14 and S18). Moreover, we allowed for correlated residuals over time, as suggested for longitudinal models [111].
Using the model describe above, we found a high stability of the modality-specific integrity estimates for each region across time (see *Results* Figure 3 and S20). Comparable to our cross-sectional analyses, we thus again added multimodal integrity factors for the LC and SN–VTA for each time point (TP1, TP2). If the multimodal integrity factors indeed remove measurement error [85], we should observe a higher stability across time points of the multimodal as compared to the modality-specific integrity factors. To test this hypothesis, we computed the covariance between the multimodal factors of TP1 and TP2 (see Figures S15 and S19). In addition, we directly compared the stability estimates, our reliability proxy, for the modality-specific and multimodal SN–VTA and LC factors. Note that the modality-specific and multimodal integrity models including TP1 and TP2 were fit across younger and older adults to obtain a single reliability proxy for the complete sample.

Assessment of within-person changes:

Previous cross-sectional research observed between-person age differences in catecholaminergic nuclei integrity [75,76], however, longitudinal studies that evaluate within-person changes in the SN–VTA and

LC are scarce. Making use of the imaging data of both time points (TP1, TP2), we thus estimated changes in catecholaminergic nuclei using latent change score models [87,149] for each imaging modality (MT+, MT–). Note that the FSE sequence was only acquired at TP2; precluding change analyses (see Table 1). To reduce model complexity, we averaged intensity ratios across hemispheres for these models. Comparable to our longitudinal cognitive analyses, we first evaluated whether the change in each region was shared across imaging modalities (i.e., sequence independent) by computing the covariance of the modality-specific slope terms (see Figures S16 and S21).
For the SN–VTA as well as the LC we observed that the changes were indeed correlated across imaging modalities (MT+, MT–). Thus, in a second set of models, we introduced a higher order multimodal slope factor to capture the shared variance across modality-specific slope factors (see Figures S17 and S22).

Longitudinal neuro–cognitive models:

In older adults, we found that SN–VTA and LC integrity changed across time (TP1–TP2; see *Longitudinal neural models*). To evaluate the behavioral implications of these changes, we leveraged a previously established cognitive factor structure [131,135] (see *Cross-sectional cognitive models*). Specifically, we were interested in testing whether changes in catecholaminergic nuclei (TP1–TP2) could be used to predict future cognition (at TP3). For this, we unified our neural change models (see Figures S17 and S22) with models of working memory and episodic memory (at TP3; cf. Figure S9). In the unified model, we specified regression paths from the neural change factors to the cognitive factors (SN–VTA to working memory; LC to episodic memory). Finally, we added chronological age (at TP2) as an additional predictor to test (1) whether catecholaminergic nuclei explains future cognition over and above age and (2) how changes in catecholaminergic nuclei differ in old age (see Figures S29 and S30). Note that cognition at TP3 was only assessed for older adults. Thus, we specified single-group models excluding younger adults.

Control analyses:

Catecholaminergic neuromodulation influences neural processing in the medial temporal lobe, a key node of the memory network [36,38,42,44,46,47]. Moreover, catecholaminergic nuclei have direct projections to the medial temporal lobe [42,44,150,151] and their integrity has been linked to tau pathology in these areas [68–70]. Thus, as a control analysis, we additionally evaluated medial temporal lobe volumes (at TP2). This allowed us to compare our measures of catecholaminergic nuclei and their association with memory performance to those of a well-established player in the memory network [109].

Voxel-based morphometry assessment:

Whole-brain MPRAGE images were processed using the voxel-based morphometry pipeline in SPM12 in MATLAB [142,152]. First, images were segmented into distinct tissue classes (e.g., grey matter, white matter, cerebrospinal fluid) using SPM12's Unified Segmentation procedure [153]. Next, a study-specific DARTEL template was created and segmented images were aligned to the template, followed by spatial normalization, modulation, and smoothing with a 2 mm full-width at half-maximum isotropic Gaussian kernel [154,155]. The resulting normalized, modulated, and smoothed grey matter images were used to derive region-of-interest volumes. Region-of-interest masks from the AAL3 atlas were applied to processed grey matter images using native SPM functions and the get_totals script (http://www0.cs.ucl.ac.uk/staff/g.ridgway/vbm/get_totals.m) to calculate volumes for the

783 parahippocampal and hippocampal regions [156]. Outlier values exceeding ± 3 standard deviations were
784 dropped, while all other values were linearly scaled (× 10,000) to facilitate subsequent model estimation.
785 Before analyses, volume data were adjusted by dividing regional estimates by total intracranial volume.

786 Cross-sectional neuro–cognitive models including voxel-based morphometry factor:

787 Mimicking our integrity factors of catecholaminergic nuclei (see Figure S3), we aggregated across left
788 and right hemispheric volumes to estimate latent parahippocampal and hippocampal factors for older
789 adults. We specified a covariance between the two regions to evaluate their association (see Figure S5).
790 We observed that parahippocampal and hippocampal factors were highly correlated (see *Supplementary*
791 *results*). Thus, we introduced a higher-order medial temporal lobe factor to capture their shared variance,
792 which we then included in our neuro-cognitive models (see *Cross-sectional neuro–cognitive models*).
793 Specifically, for older adults we estimated one correlation model and one regression model [85]. In each
794 model, we compared the associations of catecholaminergic nuclei and cognition with the medial temporal
795 lobe–cognition association (see Figures 6 and S12, S13). In addition, we quantified the interrelations of
796 SN–VTA and LC integrity and medial temporal lobe volume by estimating their covariance.

797 Data availability

798 The data that our results are based on are available from the BASE-II steering committee upon approved
799 research proposal (see https://www.base2.mpg.de/en). For inquiries, please contact Dr. Ludmilla Müller,
800 BASE-II project coordinator (lmueller@mpib-berlin.mpg.de).
801 To facilitate comparability of study results, we share the group templates with sensitivity for
802 catecholaminergic nuclei (FSE, MT+, MT–) in MNI 0.5 mm linear space (https://osf.io/eph9a/) [94].
803 The LC consensus volume of interest (LC meta mask and pontine reference mask) is available via
804 https://osf.io/sf2ky/ [90].
805 We provide two synthetic datasets of simulated cases (n = 250) that follow the population described in
806 our models, with the parameter values displayed in the model visualizations (generated using [143]). In
807 combination with the model code (see below), these data allow reproduction of key results.

808 Code availability

809 All statistical models that our inferences are based on and their outputs are available via:
810 https://osf.io/eph9a [94]
811 Vector-graphics visualizations for all models are also available via OSF.
812 Additional custom code used for processing behavioral and neural data are available from the
813 corresponding authors upon request.

Competing interests:

The authors declare no competing interests.

Acknowledgements:

This article uses data from the Berlin Aging Study II (BASE-II), which was supported by the German Federal Ministry of Education and Research (Bundesministerium für Bildung und Forschung, BMBF) under grant numbers #16SV5536 K, #16SV5537, #16SV5538, and #16SV5837, #01UW070 and #01UW0808. Additional contributions (e.g., financial, equipment, logistics, personnel) are made from each of the other participating sites, i.e., the Max Planck Institute for Human Development (MPIB), Max Planck Institute for Molecular Genetics (MPIMG), Charite-Universiätsmedizin, University Medicine, German Institute for Economic Research (DIW), Humboldt-Universität zu Berlin, all located in Berlin, Germany, and University of Lübeck, and University of Tübingen, Germany. For further information about the BASE-II project, see https://www.base2.mpg.de/en

MW-B received support from the German Research Foundation (DFG, WE 4269/5-1) and the Jacobs Foundation (Early Career Research Fellowship 2017–2019).

MM's work was supported by an Alexander von Humboldt fellowship and by National Institutes of Health grant R01AG025340.

SB was supported by a National Institutes of Health grant T32AG000037 and a National Science Foundation Grant DGE-1842487.

SD received funding from the National Science Foundation (DGE1418060).

The funders had no role in study design, data collection and analysis, decision to publish, or preparation of the manuscript.

We thank Dr. Clifford Cassidy for providing the substantia nigra and crus cerebri masks [58]. We are grateful to Dr. Ylva Köhncke and Dr. Sarah Polk for preprocessing the cognitive data.

We thank Sumedha Attanti for visually inspecting the VBM-processed segmentations.

References:

1 Nyberg, L. *et al.* (2012) Memory aging and brain maintenance. *Trends Cogn. Sci.* 16, 292–305

2 Sander, M.C. *et al.* (2012) Lifespan age differences in working memory: A two-component framework. *Neurosci. Biobehav. Rev.* 36, 2007–2033

3 Gazzaley, A. and Nobre, A.C. Top-down modulation: Bridging selective attention and working memory. , *Trends in Cognitive Sciences*, 16. 01-Feb-(2012) , Elsevier Current Trends, 129–135

4 Hasher, L. and Zacks, R.T. (1988) Working memory, comprehension, and aging: A review and a new view. *Psychol. Learn. Motiv. - Adv. Res. Theory* 22, 193–225

5 Shing, Y.L. *et al.* (2010) Episodic memory across the lifespan: The contributions of associative and strategic components. *Neurosci. Biobehav. Rev.* 34, 1080–1091

6 Tulving, E. (1983) *Elements of episodic memory*, Clarendon Press.

7 Bäckman, L. *et al.* (2006) The correlative triad among aging, dopamine, and cognition: Current status and future prospects. *Neurosci. Biobehav. Rev.* 30, 791–807

8 Li, S.-C. *et al.* (2001) Aging cognition: From neuromodulation to representation. *Trends Cogn. Sci.* 5, 479–486

9 Braver, T.S. and Barch, D.M. (2002) A theory of cognitive control, aging cognition, and neuromodulation. *Neurosci. Biobehav. Rev.* 26, 809–817

10 Mather, M. and Harley, C.W. (2016) The locus coeruleus: Essential for maintaining cognitive function and the aging brain. *Trends Cogn. Sci.* 20, 214–226

11 Weinshenker, D. (2018) Long road to ruin: Noradrenergic dysfunction in neurodegenerative disease. *Trends Neurosci.* 41, 211–223

12 Arnsten, A.F.T. *et al.* (2012) Neuromodulation of thought: flexibilities and vulnerabilities in prefrontal cortical network synapses. *Neuron* 76, 223

13 Braak, H. *et al.* (2011) Stages of the pathologic process in Alzheimer disease: Age categories from 1 to 100 years. *J. Neuropathol. Exp. Neurol.* 70, 960–969

14 Marien, M.R. *et al.* (2004) Noradrenergic mechanisms in neurodegenerative diseases: A theory. *Brain Res. Rev.* 45, 38–78

15 Matchett, B.J. *et al.* (2021) The mechanistic link between selective vulnerability of the locus coeruleus and neurodegeneration in Alzheimer's disease. *Acta Neuropathol.* 1, 3

16 Lyness, S.A. *et al.* (2003) Neuron loss in key cholinergic and aminergic nuclei in Alzheimer disease: A meta-analysis. *Neurobiol. Aging* 24, 1–23

17 Lee, J.-Y. *et al.* (2022) Multimodal brain and retinal imaging of dopaminergic degeneration in Parkinson disease. *Nat. Rev. Neurol. 2022* 0123456789, 1–18

18 Ehrenberg, A.J. *et al.* (2023) Priorities for research on neuromodulatory subcortical systems in Alzheimer's disease: Position paper from the NSS PIA of ISTAART. *Alzheimer's Dement.* 8, 21

19 Aarsland, D. *et al.* (2021) Parkinson disease-associated cognitive impairment. *Nat. Rev. Dis. Prim. 2021 71* 7, 1–21

20 Knopman, D.S. *et al.* (2021) Alzheimer disease. *Nat. Rev. Dis. Prim.* 7, 33

21 Lőrincz, M.L. and Adamantidis, A.R. (2017) Monoaminergic control of brain states and sensory processing: Existing knowledge and recent insights obtained with optogenetics. *Prog. Neurobiol.* 151, 237–253

22 Düzel, E. *et al.* (2009) Functional imaging of the human dopaminergic midbrain. *Trends Neurosci.* 32, 321–328

23 Poe, G.R. *et al.* (2020) Locus coeruleus: a new look at the blue spot. *Nat. Rev. Neurosci.* 21, 644–659

24 Servan-Schreiber, D. *et al.* (1990) A network model of catecholamine effects: Gain, signal-to-noise ratio, and behavior. *Science (80-.).* 249, 892–5

25 Thiele, A. and Bellgrove, M.A. (2018) Neuromodulation of attention. *Neuron* 97, 769–785

26 Aston-Jones, G. and Cohen, J.D. (2005) An integrative theory of locus coeruleus-norepinephrine function: Adaptive gain and optimal performance. *Annu. Rev. Neurosci.* 28, 403–450

27 Mather, M. *et al.* (2016) Norepinephrine ignites local hotspots of neuronal excitation: How arousal amplifies selectivity in perception and memory. *Behav. Brain Sci.* 39, e200
28 Koen, J.D. and Rugg, M.D. (2019) Neural dedifferentiation in the aging brain. *Trends Cogn. Sci.* 23, 547–559
29 Robbins, T.W. and Arnsten, A.F.T. (2009) The neuropsychopharmacology of fronto-executive function: Monoaminergic modulation. *Annu. Rev. Neurosci.* 32, 267–287
30 Cools, R. and Arnsten, A.F.T. (2021) Neuromodulation of prefrontal cortex cognitive function in primates: the powerful roles of monoamines and acetylcholine. *Neuropsychopharmacology* DOI: 10.1038/s41386-021-01100-8
31 Goldman-Rakic, P.S. (1995) Cellular basis of working memory. *Neuron* 14, 477–485
32 Wang, M. *et al.* (2011) Neuronal basis of age-related working memory decline. *Nature* 476, 210–213
33 Arnsten, A.F.T. and Goldman-Rakic, P.S. (1985) Alpha 2-adrenergic mechanisms in prefrontal cortex associated with cognitive decline in aged nonhuman primates. *Science (80-.).* 230, 1273–1276
34 Arnsten, A.F.T. and Contant, T.A. (1992) Alpha-2 adrenergic agonists decrease distractibility in aged monkeys performing the delayed response task. *Psychopharmacology (Berl).* 108, 159–69
35 Cai, J.X. and Arnsten, A.F.T. (1997) Dose-dependent effects of the dopamine D1 receptor agonists A77636 or SKF81297 on Spatial working memory in aged monkeys. *J. Pharmacol. Exp. Ther.* 283, 183 LP – 189
36 Lisman, J.E. and Grace, A.A. The hippocampal-VTA loop: Controlling the entry of information into long-term memory. , *Neuron*, 46. 02-Jun-(2005) , Neuron, 703–713
37 O'Dell, T.J. *et al.* (2015) β-Adrenergic receptor signaling and modulation of long-term potentiation in the mammalian hippocampus. *Learn. Mem.* 22, 461–471
38 Sara, S.J. (2009) The locus coeruleus and noradrenergic modulation of cognition. *Nat. Rev. Neurosci.* 10, 211–223
39 Lisman, J. *et al.* (2011) A neoHebbian framework for episodic memory; role of dopamine-dependent late LTP. *Trends Neurosci.* 34, 536–547
40 Hagena, H. *et al.* (2016) β-adrenergic control of pippocampal function: Subserving the choreography of synaptic information storage and memory. *Cereb. Cortex* 26, 1349–1364
41 Gruber, M.J. and Ranganath, C. (2019) How curiosity enhances hippocampus-dependent memory: The prediction, appraisal, curiosity, and exploration (PACE) Framework. *Trends Cogn. Sci.* 23, 1014–1025
42 Takeuchi, T. *et al.* (2016) Locus coeruleus and dopaminergic consolidation of everyday memory. *Nature* 537, 357–362
43 Kempadoo, K.A. *et al.* (2016) Dopamine release from the locus coeruleus to the dorsal hippocampus promotes spatial learning and memory. *Proc. Natl. Acad. Sci. U. S. A.* 113, 14835–14840
44 Tsetsenis, T. *et al.* (2021) Midbrain dopaminergic innervation of the hippocampus is sufficient to modulate formation of aversive memories. *Proc. Natl. Acad. Sci.* 118, e2111069118
45 Eisenhofer, G. (2004) Catecholamine metabolism: A contemporary view with implications for physiology and medicine. *Pharmacol. Rev.* 56, 331–349
46 Wagatsuma, A. *et al.* (2018) Locus coeruleus input to hippocampal CA3 drives single-trial learning of a novel context. *Proc. Natl. Acad. Sci. U. S. A.* 115, E310–E316
47 Duszkiewicz, A.J. *et al.* (2019) Novelty and dopaminergic modulation of memory persistence: A tale of two systems. *Trends Neurosci.* 42, 102–114
48 Chowdhury, A. *et al.* (2022) A locus coeruleus-dorsal CA1 dopaminergic circuit modulates memory linking. *Neuron* DOI: 10.1016/J.NEURON.2022.08.001
49 Burke, S.N. and Barnes, C.A. (2006) Neural plasticity in the ageing brain. *Nat. Rev. Neurosci. 2006 71* 7, 30–40
50 Barnes, C.A. (2003) Long-term potentiation and the ageing brain. *Philos. Trans. R. Soc. B Biol.*

Sci. 358, 765
51 Lubec, J. *et al.* (2021) Reinstatement of synaptic plasticity in the aging brain through specific dopamine transporter inhibition. *Mol. Psychiatry* 26, 7076–7090
52 Astafiev, S. V. *et al.* (2010) Comment on "Modafinil shifts human locus coeruleus to low-tonic, high-phasic activity during functional MRI" and "Homeostatic sleep pressure and responses to sustained attention in the suprachiasmatic area." *Science (80-.).* 328, 309
53 Keren, N.I. *et al.* (2009) In vivo mapping of the human locus coeruleus. *Neuroimage* 47, 1261–1267
54 Sulzer, D. *et al.* (2018) Neuromelanin detection by magnetic resonance imaging (MRI) and its promise as a biomarker for Parkinson's disease. *npj Park. Dis.* 4, 11
55 Liu, K.Y. *et al.* (2017) Magnetic resonance imaging of the human locus coeruleus: A systematic review. *Neurosci. Biobehav. Rev.* 83, 325–355
56 Betts, M.J. *et al.* (2019) Locus coeruleus imaging as a biomarker for noradrenergic dysfunction in neurodegenerative diseases. *Brain* 142, 2558–2571
57 Keren, N.I. *et al.* (2015) Histologic validation of locus coeruleus MRI contrast in post-mortem tissue. *Neuroimage* 113, 235–245
58 Cassidy, C.M. *et al.* (2019) Neuromelanin-sensitive MRI as a noninvasive proxy measure of dopamine function in the human brain. *Proc. Natl. Acad. Sci. U. S. A.* 116, 5108–5117
59 Kitao, S. *et al.* (2013) Correlation between pathology and neuromelanin MR imaging in Parkinson's disease and dementia with Lewy bodies. *Neuroradiology* 55, 947–953
60 Zecca, L. *et al.* (2004) The role of iron and copper molecules in the neuronal vulnerability of locus coeruleus and substantia nigra during aging. *Proc. Natl. Acad. Sci. U. S. A.* 101, 9843–9848
61 Zucca, F.A. *et al.* (2017) Interactions of iron, dopamine and neuromelanin pathways in brain aging and Parkinson's disease. *Prog. Neurobiol.* 155, 96–119
62 Carballo-Carbajal, I. *et al.* (2019) Brain tyrosinase overexpression implicates age-dependent neuromelanin production in Parkinson's disease pathogenesis. *Nat. Commun.* 10, 973
63 Trujillo, P. *et al.* (2017) Contrast mechanisms associated with neuromelanin-MRI. *Magn. Reson. Med.* 78, 1790–1800
64 Simpson, K.L. and Lin, R.C.S. (2007) Neuroanatomical and chemical organization of the locus coeruleus. In *Brain Norepinephrine* (Ordway, G. A. et al., eds), pp. 9–52, Cambridge University Press
65 Watanabe, T. *et al.* (2019) Magnetic resonance imaging of noradrenergic neurons. *Brain Struct. Funct.* 224, 1609–1625
66 Priovoulos, N. *et al.* (2020) Unraveling the contributions to the neuromelanin-MRI contrast. *Brain Struct. Funct.* 1, 3
67 Trujillo, P. *et al.* (2019) Quantitative magnetization transfer imaging of the human locus coeruleus. *Neuroimage* 200, 191–198
68 Dahl, M.J. *et al.* (2022) Locus coeruleus integrity is related to tau burden and memory loss in autosomal-dominant Alzheimer's disease. *Neurobiol. Aging* 112, 39–54
69 Jacobs, H.I.L. *et al.* (2021) In vivo and neuropathology data support locus coeruleus integrity as indicator of Alzheimer's disease pathology and cognitive decline. *Sci. Transl. Med.* 13, eabj2511
70 Cassidy, C.M. *et al.* (2022) Association of locus coeruleus integrity with Braak stage and neuropsychiatric symptom severity in Alzheimer's disease. *Neuropsychopharmacol. 2022* DOI: 10.1038/s41386-022-01293-6
71 Gaurav, R. *et al.* (2021) Longitudinal Changes in Neuromelanin MRI Signal in Parkinson's Disease: A Progression Marker. *Mov. Disord.* 36, 1592–1602
72 Matsuura, K. *et al.* (2016) A longitudinal study of neuromelanin-sensitive magnetic resonance imaging in Parkinson's disease. *Neurosci. Lett.* 633, 112–117
73 Braak, H. *et al.* (2003) Staging of brain pathology related to sporadic Parkinson's disease. *Neurobiol. Aging* 24, 197–211
74 Brettschneider, J. *et al.* Spreading of pathology in neurodegenerative diseases: A focus on human

studies. , *Nature Reviews Neuroscience*, 16. 01-Jan-(2015) , Nature Publishing Group, 109–120
75 Liu, K.Y. *et al.* (2019) In vivo visualization of age-related differences in the locus coeruleus. *Neurobiol. Aging* 74, 101–111
76 Shibata, E. *et al.* (2006) Age-related changes in locus coeruleus on neuromelanin magnetic resonance imaging at 3 Tesla. *Magn. Reson. Med. Sci.* 5, 197–200
77 Xing, Y. *et al.* (2018) Life span pigmentation changes of the substantia nigra detected by neuromelanin-sensitive MRI. *Mov. Disord.* 33, 1792–1799
78 Jacobs, H.I.L. *et al.* (2021) Alzheimer's disease pathology: pathways between central norepinephrine activity, memory, and neuropsychiatric symptoms. *Mol. Psychiatry* 26, 897–906
79 Jacobs, H.I.L. *et al.* (2022) Waning locus coeruleus integrity precedes cortical tau accrual in preclinical autosomal dominant Alzheimer's disease. *Alzheimers. Dement.* DOI: 10.1002/ALZ.12656
80 Delius, J.A.M. *et al.* (2015) Berlin Aging Studies (BASE and BASE-II). In *Encyclopedia of geropsychology* (Pachana, N. A., ed), pp. 386–395, Springer
81 Gerstorf, D. *et al.* (2016) The Berlin Aging Study II: An overview [Editorial]. *Gerontology* 62, 311–315
82 Bertram, L. *et al.* (2014) Cohort profile: The Berlin Aging Study II (BASE-II). *Int. J. Epidemiol.* 43, 703–712
83 Demuth, I. *et al.* (2021) Cohort profile: follow-up of a Berlin Aging Study II (BASE-II) subsample as part of the GendAge study. *BMJ Open* 11, e045576
84 Kühn, S. *et al.* (2017) In search of features that constitute an "enriched environment" in humans: Associations between geographical properties and brain structure. *Sci. Rep.* 7, 1–8
85 Köhncke, Y. *et al.* (2021) Hippocampal and Parahippocampal Gray Matter Structural Integrity Assessed by Multimodal Imaging Is Associated with Episodic Memory in Old Age. *Cereb. Cortex* 31, 1464–1477
86 Düzel, S. *et al.* (2016) The Subjective Health Horizon Questionnaire (SHH-Q): Assessing Future Time Perspectives for Facets of an Active Lifestyle. *Gerontology* 62, 345–353
87 Kievit, R.A. *et al.* (2018) Developmental cognitive neuroscience using latent change score models: A tutorial and applications. *Dev. Cogn. Neurosci.* 33, 99–117
88 Dahl, M.J. *et al.* (2019) Rostral locus coeruleus integrity is associated with better memory performance in older adults. *Nat. Hum. Behav.* 3, 1203–1214
89 Gallant, S.N. *et al.* (2022) Behavioral and fMRI evidence that arousal enhances bottom-up selectivity in young but not older adults. *Neurobiol. Aging* DOI: 10.1016/J.NEUROBIOLAGING.2022.08.006
90 Dahl, M.J. *et al.* (2022) Locus coeruleus integrity is related to tau burden and memory loss in autosomal-dominant Alzheimer's disease. *Neurobiol. Aging* 112, 39–54
91 Bachman, S.L. *et al.* (2022) Daily heart rate variability biofeedback training decreases locus coeruleus MRI contrast in younger adults. *medRxiv* DOI: 10.1101/2022.02.04.22270468
92 Giorgi, F.S. *et al.* (2022) Locus Coeruleus magnetic resonance imaging: a comparison between native-space and template-space approach. *J. Neural Transm. 2022* 1, 1–8
93 Polk, S.E. *et al.* (2022) Change in latent gray-matter structural integrity is associated with change in cardiovascular fitness in older Adults who engage in at-home aerobic exercise. *Front. Hum. Neurosci.* 16,
94 Dahl, M.J. *et al.* (2022) The integrity of dopaminergic and noradrenergic brain regions is associated with different aspects of late-life memory performance. *OSF* DOI: https://doi.org/10.17605/OSF.IO/EPH9A
95 Brandmaier, A.M. *et al.* (2018) Precision, reliability, and effect size of slope variance in latent growth curve models: Implications for statistical power analysis. *Front. Psychol.* 9, 294
96 Eid, M. *et al.* (2015) *Statistik und Forschungsmethoden: Lehrbuch*, Beltz.
97 Briand, L.A. *et al.* (2007) Modulators in concert for cognition: Modulator interactions in the prefrontal cortex. *Prog. Neurobiol.* 83, 69–91

98 Elman, J.A. *et al.* (2021) MRI-assessed locus coeruleus integrity is heritable and associated with cognition, Alzheimer's risk, and sleep-wake disturbance. *Alzheimer's Dement.* 17, 1017– 1025
99 Liu, K.Y. *et al.* (2020) Noradrenergic-dependent functions are associated with age-related locus coeruleus signal intensity differences. *Nat. Commun.* 11, 1712
100 Allen, M. *et al.* (2021) Raincloud plots: a multi-platform tool for robust data visualization. *Wellcome Open Res. 2021 463* 4, 63
101 Ehrenberg, A.J. *et al.* (2017) Quantifying the accretion of hyperphosphorylated tau in the locus coeruleus and dorsal raphe nucleus: The pathological building blocks of early Alzheimer's disease. *Neuropathol. Appl. Neurobiol.* 43, 393–408
102 Stratmann, K. *et al.* (2016) Precortical phase of Alzheimer's disease (AD)-related tau cytoskeletal pathology. *Brain Pathol.* 26, 371–386
103 Theofilas, P. *et al.* (2015) Turning on the light within: Subcortical nuclei of the isodentritic core and their role in Alzheimer's disease pathogenesis. *J. Alzheimer's Dis.* 46, 17–34
104 Chalermpalanupap, T. *et al.* (2017) Down but not out: The consequences of pretangle tau in the locus coeruleus. *Neural Plast.* 2017, 7829507
105 Ghosh, A. *et al.* (2019) An experimental model of Braak's pretangle proposal for the origin of Alzheimer's disease: The role of locus coeruleus in early symptom development. *Alzheimer's Res. Ther.* 11, 59
106 Rorabaugh, J.M. *et al.* (2017) Chemogenetic locus coeruleus activation restores reversal learning in a rat model of Alzheimer's disease. *Brain* 140, 3023–3038
107 Feinstein, D.L. *et al.* (2002) Noradrenergic regulation of inflammatory gene expression in brain. *Neurochem. Int.* 41, 357–365
108 Rommelfanger, K.S. and Weinshenker, D. (2007) Norepinephrine: The redheaded stepchild of Parkinson's disease. *Biochem. Pharmacol.* 74, 177–190
109 Moscovitch, M. *et al.* (2016) Episodic memory and beyond: The hippocampus and neocortex in transformation. *Annu. Rev. Psychol.* 67, 105–134
110 Bunzeck, N. *et al.* (2007) Mesolimbic novelty processing in older adults. *Cereb. Cortex* 17, 2940–2948
111 Little, T.D. (2013) *Longitudinal structural equation modeling.*, Guilford Press.
112 Wilson, R.S. *et al.* (2013) Neural reserve, neuronal density in the locus ceruleus, and cognitive decline. *Neurology* 80, 1202–1208
113 Seiler, S. *et al.* (2014) Magnetization Transfer Imaging for in vivo Detection of Microstructural Tissue Changes in Aging and Dementia: A Short Literature Review. *J. Alzheimer's Dis.* 42, S229–S237
114 Tona, K.D. *et al.* (2017) In vivo visualization of the locus coeruleus in humans: Quantifying the test–retest reliability. *Brain Struct. Funct.* 222, 4203–4217
115 Allen, R.J. *et al.* (2022) Intact high-resolution working memory binding in a patient with developmental amnesia and selective hippocampal damage. *Hippocampus* 32, 597–609
116 Ciampa, C.J. *et al.* (2022) Associations among locus coeruleus catecholamines, tau pathology, and memory in aging. *Neuropsychopharmacol. 2022* DOI: 10.1038/s41386-022-01269-6
117 Biondetti, E. *et al.* (2020) Spatiotemporal changes in substantia nigra neuromelanin content in Parkinson's disease. *Brain* 143, 2757–2770
118 Corbetta, M. *et al.* (2008) The reorienting system of the human brain: From environment to theory of mind. *Neuron* 58, 306–324
119 Bouret, S. and Sara, S.J. (2005) Network reset: A simplified overarching theory of locus coeruleus noradrenaline function. *Trends Neurosci.* 28, 574–582
120 Sara, S.J. and Bouret, S. (2012) Orienting and reorienting: The locus coeruleus mediates cognition through arousal. *Neuron* 76, 130–141
121 Privitera, M. *et al.* (2020) A complete pupillometry toolbox for real-time monitoring of locus coeruleus activity in rodents. *Nat. Protoc.* 15, 2301–2320
122 Vazey, E.M. *et al.* (2018) Phasic locus coeruleus activity regulates cortical encoding of salience

information. *Proc. Natl. Acad. Sci. U. S. A.* 115, E9439–E9448
123 Joshi, S. and Gold, J.I. (2020) Pupil size as a window on neural substrates of cognition. *Trends Cogn. Sci.* 24, 466–480
124 Dahl, M.J. *et al.* (2020) Noradrenergic responsiveness supports selective attention across the adult lifespan. *J. Neurosci.* 40, 4372–4390
125 Dahl, M.J. *et al.* (2022) Noradrenergic modulation of rhythmic neural activity shapes selective attention. *Trends Cogn. Sci.* 26, 38–52
126 Theofilas, P. *et al.* (2017) Locus coeruleus volume and cell population changes during Alzheimer's disease progression: A stereological study in human postmortem brains with potential implication for early-stage biomarker discovery. *Alzheimer's Dement.* 13, 236–246
127 David, M.C.B. *et al.* (2022) Cognitive and neuropsychiatric effects of noradrenergic treatment in Alzheimer's disease: systematic review and meta-analysis. *J. Neurol. Neurosurg. Psychiatry* 0, jnnp-2022-329136
128 O'Callaghan, C. *et al.* (2021) Locus coeruleus integrity and the effect of atomoxetine on response inhibition in Parkinson's disease. *Brain* 144, 2513–2526
129 Sherpa, A.D. *et al.* (2016) Activation of β-adrenergic receptors in rat visual cortex expands astrocytic processes and reduces extracellular space volume. *Synapse* 70, 307–316
130 Xie, L. *et al.* (2013) Sleep Drives Metabolite Clearance from the Adult Brain. *Science* 342, 373–377
131 Düzel, S. *et al.* (2016) The Subjective Health Horizon Questionnaire (SHH-Q): Assessing Future Time Perspectives for Facets of an Active Lifestyle. *Gerontology* 62, 345–353
132 Lindenberger, U. *et al.* (1993) Speed and intelligence in old age. *Psychol. Aging* 8, 207–220
133 Schmiedek, F. *et al.* (2010) Hundred days of cognitive training enhance broad cognitive abilities in adulthood: Findings from the COGITO study. *Front. Aging Neurosci.* 2,
134 Lindenberger, U. *et al.* (1993) Speed and intelligence in old age. *Psychol. Aging* 8, 207–220
135 Kühn, S. *et al.* (2019) Food for thought: association between dietary tyrosine and cognitive performance in younger and older adults. *Psychol. Res.* 83, 1097–1106
136 Chen, X. *et al.* (2014) Simultaneous imaging of locus coeruleus and substantia nigra with a quantitative neuromelanin MRI approach. *Magn. Reson. Imaging* 32, 1301–1306
137 Bachman, S.L. *et al.* (2022) Daily heart rate variability biofeedback training decreases locus coeruleus MRI contrast in younger adults. *medRxiv* DOI: 10.1101/2022.02.04.22270468
138 Avants, B.B. *et al.* (2009) Advanced Normalization Tools: V1.0. *Insight J.* 2,
139 Avants, B.B. *et al.* (2011) A reproducible evaluation of ANTs similarity metric performance in brain image registration. *Neuroimage* 54, 2033–2044
140 Ciric, R. *et al.* (2021) TemplateFlow: a community archive of imaging templates and atlases for improved consistency in neuroimaging. *bioRxiv* DOI: 10.1101/2021.02.10.430678
141 Smith, S.M. (2002) Fast robust automated brain extraction. *Hum. Brain Mapp.* 17, 143–155
142 Friston, K. *et al.* (2007) *Statistical Parametric Mapping: The Analysis of Functional Brain Images*, 1st edn.Academic Press.
143 von Oertzen, T. *et al.* (2015) Structural equation modeling with Ωnyx. *Struct. Equ. Model.* 22, 148–161
144 Rosseel, Y. (2012) Lavaan: An R package for structural equation modeling. *J. Stat. Softw.* 48, 1–36
145 Brown, T.A. (2006) *Confirmatory factor analysis for applied research*, Guilford Press.
146 Hu, L.T. and Bentler, P.M. (1999) Cutoff criteria for fit indexes in covariance structure analysis: Conventional criteria versus new alternatives. *Struct. Equ. Model.* 6, 1–55
147 Meredith, W. and Teresi, J.A. (2006) An essay on measurement and factorial invariance. *Med. Care* 44, S69–S77
148 Kline, R.B. (2016) *Principles and practice of structural equation modeling, 4th ed.*, Guilford Press.
149 McArdle, J.J. (2009) Latent variable modeling of differences and changes with longitudinal data.

Annu. Rev. Psychol. 60, 577–605

150 Solders, S.K. *et al.* (2021) Diffusion MRI tractography of the locus coeruleus-transentorhinal cortex connections using GO-ESP. *Magn. Reson. Med.* 00, 1–16

151 Porat, S. *et al.* (2022) Age differences in diffusivity in the locus coeruleus and its ascending noradrenergic tract. *Neuroimage* 251, 119022

152 Ashburner, J. and Friston, K.J. (2000) Voxel-based morphometry - The methods. *Neuroimage* 11, 805–821

153 Ashburner, J. and Friston, K.J. (2005) Unified segmentation. *Neuroimage* 26, 839–851

154 Ashburner, J. (2007) A fast diffeomorphic image registration algorithm. *Neuroimage* 38, 95–113

155 Ashburner, J. and Friston, K.J. (2009) Computing average shaped tissue probability templates. *Neuroimage* 45, 333–341

156 Rolls, E.T. *et al.* (2020) Automated anatomical labelling atlas 3. *Neuroimage* 206, 116189